



Article

Mathematical Analysis of a Low Cost Mechanical Ventilator Respiratory Dynamics Enhanced by a Sensor Transducer (ST) Based in Nanostructures of Anodic Aluminium Oxide (AAO)

Jesús Alan Calderón Chavarri ^{1,2,*}, Carlos Gianpaul Rincón Ruiz ², Ana María Gómez Amador ³,
Bray Jesús Martín Agreda Cardenas ², Sebastián Calero Anaya ², John Hugo Lozano Jauregui ^{2,4},
Alexandr Toribio Hinostriza ⁴ and Juan José Jiménez de Cisneros y Fonfría ²

- ¹ Angewandte Nanophysik, Institut Für Physik, Technische Universität Ilmenau, 98693 Ilmenau, Germany
² Engineering Department, Pontificia Universidad Católica del Perú, Lima 15088, Peru; rinconr.carlos@pucp.pe (C.G.R.R.); b.agreda@pucp.edu.pe (B.J.M.A.C.); sebastian.calero@pucp.pe (S.C.A.); john.lozanoj@pucp.edu.pe (J.H.L.J.); juanjose.cisneros@pucp.pe (J.J.J.d.C.y.F.)
³ Department of Mechanical Engineering, Universidad Carlos III de Madrid, 28911 Madrid, Spain; amgomez@ing.uc3m.es
⁴ Mechatronic Department, Northen (Arctic) Federal University Named after M.V. Lomonosov, Arkhangelsk 163002, Russia; alexandrtoribio@mail.ru
* Correspondence: alan.calderon@pucp.edu.pe



Citation: Chavarri, J.A.C.; Ruiz, C.G.R.; Gómez Amador, A.M.; Cardenas, B.J.M.A.; Anaya, S.C.; Lozano Jauregui, J.H.; Hinostriza, A.T.; Jiménez de Cisneros y Fonfría, J.J. Mathematical Analysis of a Low Cost Mechanical Ventilator Respiratory Dynamics Enhanced by a Sensor Transducer (ST) Based in Nanostructures of Anodic Aluminium Oxide (AAO). *Mathematics* **2022**, *10*, 2403. <https://doi.org/10.3390/math10142403>

Academic Editor: James M. Buick

Received: 8 April 2022

Accepted: 19 June 2022

Published: 8 July 2022

Publisher's Note: MDPI stays neutral with regard to jurisdictional claims in published maps and institutional affiliations.



Copyright: © 2022 by the authors. Licensee MDPI, Basel, Switzerland. This article is an open access article distributed under the terms and conditions of the Creative Commons Attribution (CC BY) license (<https://creativecommons.org/licenses/by/4.0/>).

Abstract: Mechanical ventilation systems require a device for measuring the air flow provided to a patient in order to monitor and ensure the correct quantity of air proportionated to the patient, this device is the air flow sensor. At the beginning of the COVID-19 pandemic, flow sensors were not available in Peru because of the international supply shortage. In this context, a novel air flow sensor based on an orifice plate and an intelligent transducer was developed to form an integrated device. The proposed design was focused on simple manufacturing requirements for mass production in a developing country. CAD and CAE techniques were used in the design stage, and a mathematical model of the device was proposed and calibrated experimentally for the measured data transduction. The device was tested in its real working conditions and was therefore implemented in a breathing circuit connected to a low-cost mechanical ventilation system. Results indicate that the designed air flow sensor/transducer is a low-cost complete medical device for mechanical ventilators that is able to provide all the ventilation parameters by an equivalent electrical signal to directly display the following factors: air flow, pressure and volume over time. The evaluation of the designed sensor transducer was performed according to sundry transducer parameters such as geometrical parameters, material parameters and adaptive coefficients in the main transduction algorithm; in effect, the variety of the described results were achieved by the faster response time and robustness proportionated by transducers of nanostructures based on Anodic Aluminum Oxide (AAO), which enhanced the designed sensor/transducer (ST) during operation in intricate geographic places, such as the Andes mountains of Peru.

Keywords: air flow medical sensor; emergency air flow sensor; low-cost air flow sensor; nanostructures; COVID-19

MSC: 65K10

1. Introduction

Monitoring has become indispensable for mechanical ventilators in order to provide feedback to medical staff regarding treatment. Moreover, ventilation parameters can be used for internal control tasks such as adaptive feedback which improves the equipment performance and response to disturbances. Thus, appropriated values of physical variables and artificial breathing could be achieved by monitoring the ventilation curves in real

time [1]. In this sense, a flow sensor is a device used for air flow measurement, and its working concept is commonly based on an induced pressure drop across an orifice which can be measured and related to the air flow value in a breathing circuit over time [2].

Design considerations for air flow measurement in industrial applications are well established in the steady-state condition [3]; nevertheless, the air flow provided by the developed low-cost mechanical ventilator has a particular periodic waveform in a transient condition. Typical medical air flow sensors measure the pressure drop using static pressure taps connected to a transducer. However, this represents a risk of leaking polluted air from the patient, which is a harmful risk given the current pandemic context. To counter this, modern medical air flow sensors are connected to electrical transducers to generate electrical values analogous to values of static pressure [4]. Having a sensor connected to an electrical transducer is quite important for the measured variables, as their electrical equivalent values can be stored in the main control system of the ventilator. On the other hand, any kind of virus can be reduced, something that cannot be achieved with typical airflow connectors. Furthermore, air flow sensors cannot provide air pressure and volume and other parameters, which require monitoring, are measured using an additional sensor and calculated at the processing stage.

In this study, a novel air flow sensor/transducer was proposed as an integrated design that is able to measure the air flow in a breathing circuit in the time domain and estimate the air pressure and volume parameters with the mathematical model developed and calibrated experimentally for a specific low-cost mechanical ventilator based on cams [1]. This proposed medical device directly provides the equivalent electrical signals of air pressure, volume and flow after a transduction stage required due to the nonlinearity of the air flow and pressure drop [5].

During the COVID-19 pandemic, many low-cost mechanical ventilation systems based on the compression of an airbag were developed [6], but they were required to measure the generated air flow rate to the patient [7]. However, air flow sensors were not easy to resource in Peruvian markets due to the international supply shortage during this period of the pandemic. Moreover, the design and fabrication for this medical application requires certain considerations, such as those proposed in this research.

2. Materials and Methods

Broadly, the methodology consists of design, fabrication, experimental study and experimental validation stages. The design was an iterative process, thus in this paper only the final version which was improved according to the experimental results is shown. Figure 1 shows an overview of the research flow. In the design stage, sensor architecture and functions were established. The transduction algorithm correlates the theoretical pressure difference and ventilation curves shown in the display. A Computational Fluid Dynamics (CFD) analysis supports an exhaustive study of air airflow measurement in different flow conditions as well as with different orifice plate dimensions. A sensor prototype and equipment were specially designed for the experimental study. The experimental data obtained were used for the mathematical characterization of the sensor in dynamic [8], steady and real working conditions. Design improvement and model calibration were carried out based on the CFD simulation and experimental characterization [9].

Finally, the design was improved and fabricated for the experimental validation where the device measurement, connected to a mechanical ventilator, was compared to the measurement of a Fluke air flow meter.

2.1. Device Description

Figure 2 shows the sensor/transducer concept. It consists of an orifice plate sensor, a pressure transducer and a controller. The crossing air flow through the orifice plate produces a pressure difference related to the air flow value. Then, the pressure transducer converts the pressure signals into their electric equivalent signals which are sent to the

controller for data treatment in order to determine and display the pressure, volume and flow over time using an electronic screen [10].

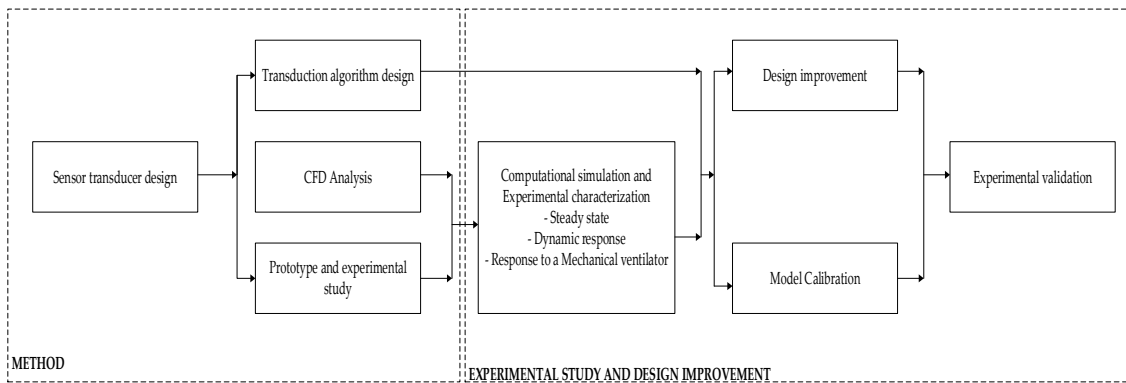


Figure 1. Research overview.

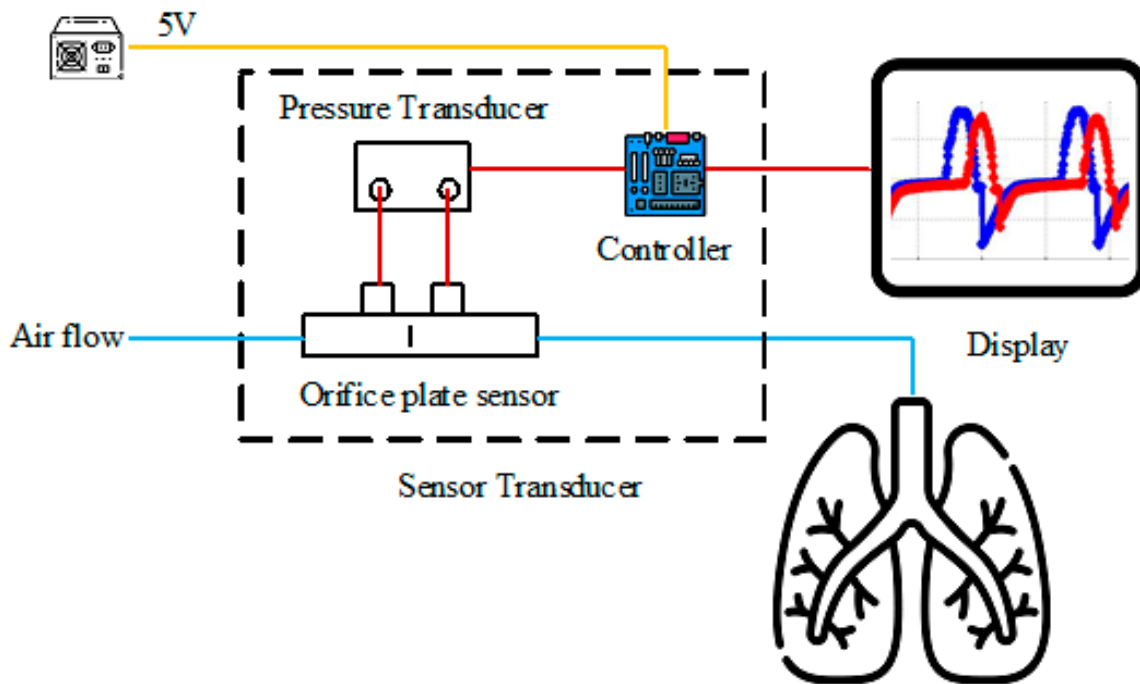


Figure 2. Scheme of the designed air flow sensor transducer.

2.2. Device Design

Figure 3 shows the integrated air flow sensor/transducer developed for this particular transient flow measurement. It consists of a compact air flow sensor based on an orifice plate and a transduction stage of the measured pressure difference over time. The transduction stage and pressure difference measurement were integrated in this device in order to prevent leaks or contaminated air flow. The device measures the air flow through it and calculates (using a microcontroller Arduino UNO) the breathing variables transduced as electrical values that are depicted on the electronic screen and sent to the main control system of the mechanical ventilator.

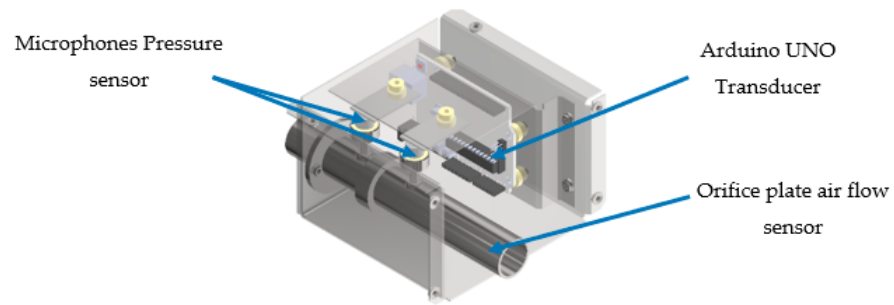


Figure 3. Design of an integrated air flow sensor/transducer for a breathing circuit.

Figure 4 shows the compact air flow sensor developed for the integrated design, which is composed of an upstream and downstream pipe welded to an orifice plate. Dimensions are established based on the analytic and experimental results, which guarantee the pressure difference measurement over time for this particular medical application with a mechanical ventilation system OxygenIP.PE, whose nominal working conditions correspond to a transient flow [11].

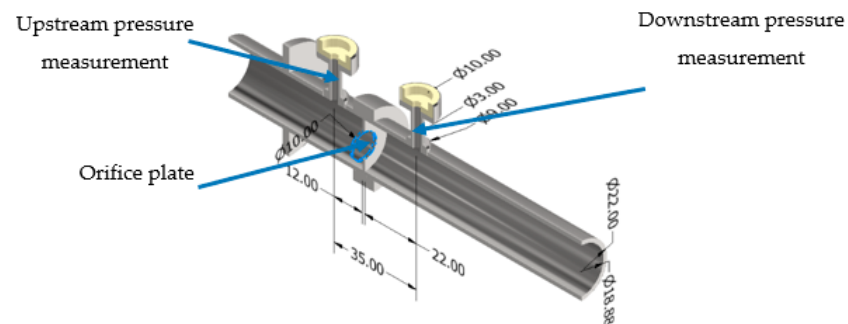


Figure 4. Compact air flow sensor developed for the air flow sensor/transducer.

2.3. Mathematical Modelling

The design of the flow sensor was based on the mathematical model analysis as a consequence of the theoretical equations, which describe the flow behavior through an orifice plate. Moreover, the analysis was enhanced due to the correlation with polynomial models that provided adaptive coefficients for the optimal measurements, for which the process is described in more detail in the following paragraphs.

In Figure 5, a scheme to explain the theoretical model of the flow inside the airflow circuit is depicted. In which f is the air flow from a source, the section area of the hose is a , and the flow reduces its section area b while crossing the orifice plate. Thus, a pressure difference can be measured between points P_1 and P_2 , moreover v_1 and v_2 represent the fluid flow speed of the air flow in the direction depicted by the red arrow [11,12].

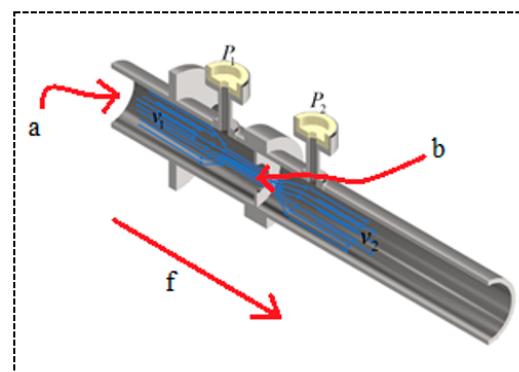


Figure 5. Scheme of the orifice plate theoretical model.

In order to find the pressure, airflow and volume equations, the Stokes equations were analyzed using Equation (1), in which, “ f ” is the function as the consequence of airflow and “ μ ” and “ D ” are the average velocity and dispersion coefficient, respectively [13,14].

$$\frac{\partial f}{\partial t} + \mu \frac{\partial f}{\partial x} = D \frac{\partial f^2}{\partial x^2} \tag{1}$$

This expression can be reduced to the Bernoulli model, and with the analysis of the energy balance, Equation (2) can be obtained [13], in which ρ is the fluid flow density, p_1 and p_2 are the initial and final referential pressure through the fluid flow path, and v_1 and v_2 are the fluid flow speed.

$$\frac{1}{2}\rho v_1^2 + p_1 = \frac{1}{2}\rho v_2^2 + p_2 \tag{2}$$

By conducting a static pressure analysis, it is possible to obtain Equation (3), where ϱ is the volumetric flow rate [13], A_1 and A_2 are the cross sections area, and the initial and the final static pressure are p_1 and p_2 , which are proportionate to the difference of pressure ΔP .

$$\Phi = A_2 \sqrt{\frac{2\Delta P}{\varrho \left(1 - \left(\frac{A_2}{A_1}\right)^2\right)}} \tag{3}$$

From here, it is further possible to reduce to the equation by considering the “discharge coefficient C_d ” so that Equation (4) is obtained [13].

$$\Phi = C_d A_2 \sqrt{\frac{2\Delta P}{\varrho \left(1 - \left(\frac{A_2}{A_1}\right)^2\right)}} \tag{4}$$

Finally, a theoretical model can be derived from the expected breathing curve as shown by Equation (5) [13], in which R_i has the geometrical and material information of the fluid flow sensor. Equation (5) proposes the relation among the volumetric flow rate Φ with the pressure difference of ΔP , and τ is the response time.

$$\Phi = \left(\frac{\Delta P}{R_i}\right) \left(1 - e^{-\frac{t}{\tau}}\right) \tag{5}$$

2.4. Computational Fluid Dynamics (CFD) Analysis

Sensor Case Setup

The geometry was modelled after the actual state bench design proposal (with an extended outlet to overcome reverse flow issues). Following Bridgeman’s steps [15], the sensor case was modelled as axisymmetric and the pressure sensing ports’ geometries were disregarded to save computational resources and time. Because of this, better and more structured meshes were obtained. Five geometries were generated in total (one for each orifice diameter). The meshes were then generated with an element size of 0.00025 m, all with good or excellent mesh metrics results, according to Ansys [16]. Figure 6 shows the model for the 10 mm orifice plate of the sensor case, in which A and B keep the distance for the static pressure orifices.

The main equations that govern this analysis are provided by the Navier–Stokes equations, mainly the x-y momentum and continuity equations. The energy equation was not included in the analysis since heat transfer was not one of the concerns of this study. The SST k- ϵ turbulence model was selected for this study because it combines the following 2 separate models: the k- ϵ and k- ϵ turbulence models. The first model is better at capturing near-the-wall turbulence effects, and the second model is superior at capturing turbulence effects away from the walls.

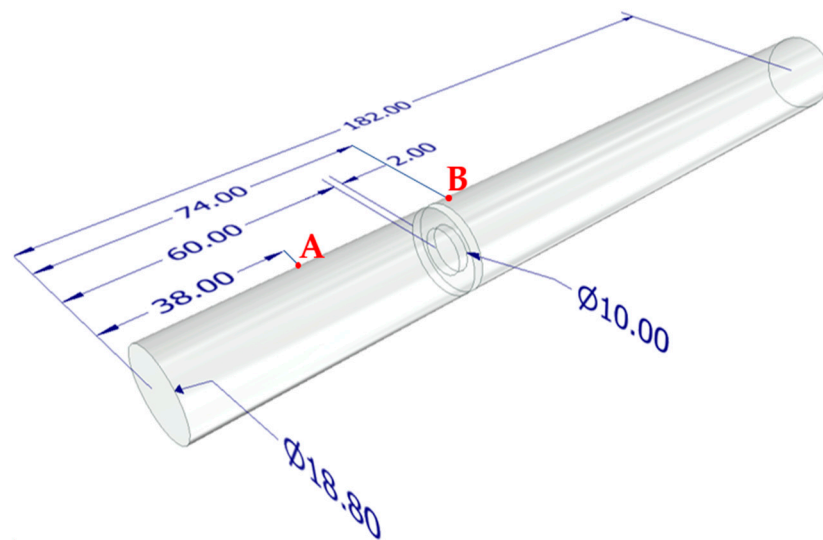


Figure 6. Sensor case geometry for 10 mm orifice plate.

The following initial and border conditions were considered:

- Air assumed as incompressible fluid [17];
- Density = 1.18 kg/m^3 ;
- Atmospheric pressure at the outlet (101,325 Pa);
- Dynamic Viscosity = $1.7984 \times 10^{-5} \text{ kg/(m-s)}$;
- No slip condition at the walls.

A mesh sensitivity analysis was performed for 3 different meshes. The first one contained 6962 elements; the second, 27,843; and the third, 43,045. The populations corresponded to meshes with element sizes of 0.0005 m, 0.00025 m, and 0.0002 m, respectively. These 3 different meshes were run as steady state cases for the 4 mm orifice and 100 L/min airflow. The results were then graphed.

Figure 7 shows that the results began to converge towards a single pressure difference value. If the mesh refining continued, a single pressure difference value would be reached. Since the geometry was simple, a highly populated mesh was not necessary. This is shown in Figure 6, where almost double the number of elements only resulted in an increase of 0.31% of the pressure difference, as well as a considerable increase of almost 6 times the required number of iterations before the residuals reached convergence. Therefore, to save computational resources and time, but at the same time still obtain acceptable results, a mesh with an element size of 0.00025 m was selected for the simulations. The mesh used for the 10 mm orifice model is shown in Figure 8.

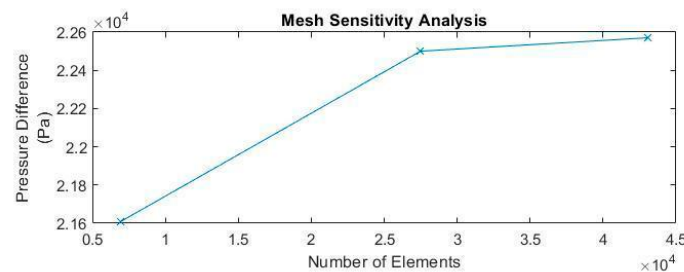


Figure 7. Mesh Sensitivity Analysis.



Figure 8. Mesh for 10 mm orifice model.

2.5. Transduction Stage Design

After studying the theoretical model with the Navier–Stokes equations and analyzing the sensor case via simulation methodologies, experiments were conducted to develop the experimental model of the designed sensor/transducer. Equations (6) and (7) represent a non-linear system, where $u(t)$ is the input signal (for example pressure from cam over pivot), $y(t)$ is the response (such as for example airflow crossing airbag to a connected hose), $x(t)$ is an internal variable which allows the connection between input signals and response, f and h represent the non-linear characteristics of the system such as functions, while θ represents physical parameters of the system and t the time. The function f contains the mechanic parameters, fluid parameters and electrical parameters for the correlation between the theoretic and experimental model of the designed sensor [1,13,18].

$$\frac{dx(t)}{dt} = f(x(t), u(t), \theta) \tag{6}$$

$$y(t) = h(x(t), u(t), \theta) \tag{7}$$

It is possible to propose the mathematical model of the system (sensor/transducer) with Equations (6) and (7) described above. Moreover, it is necessary to find the optimal signal (input variable) that provides a predicted response. Hence, Equation (8) depends on the trajectory solution as set point R_s and $r(k_i)$ is the set point of sample time k_i .

$$R_s^T = (111 \dots 11111111)r(k_i) \tag{8}$$

Equation (9) has a dependence of matrices R_s and ΔU . The optimal predicted solution for a desired value in the system is obtained based on the cost function “ J ” among optimal predicted response with this “trajectory solution Y ” such as the optimal predicted solution ΔU , which is described using Equation (9). The procedure to calculate ΔU is given by Equations (10)–(14), furthermore, R is a diagonal matrix to tune the desired optimal response matrix.

$$J = (R_s - Y)^T (R_s - Y) + \Delta U^T R \Delta U \tag{9}$$

On the other hand, the “Optimal predicted response Y ” has a dependence of “matrices F , φ and the state vector $X(k_i)$ ” as shown by Equation (10)

$$Y = FX(k_i) + \varphi \Delta U \tag{10}$$

Moreover, using the costing function “ J ” the optimal estimation was analyzed, as it is described by Equation (11) after replacing Equation (10) in Equation (9).

$$J = (R_s - FX(k_i))^T (R_s - FX(k_i)) - 2\Delta U^T \varphi^T (R_s - FX(k_i)) + \Delta U^T (\varphi^T \varphi + R) \Delta U \tag{11}$$

Looking for the minimal error, Equation (11) was derived as the dependence of “ ΔU ” in Equation (12).

$$\frac{\partial J}{\partial \Delta U} = -2\varphi^T (R_s - FX(k_i)) + 2(\varphi^T \varphi + R) \Delta U \tag{12}$$

Therefore, the minimal value of “ J ” was achieved using Equation (13).

$$\frac{\partial J}{\partial \Delta U} = 0 \tag{13}$$

This means that the optimal “ ΔU ” is given by Equation (14), which helps to obtain the optimal and predicted “ Y ”.

$$\Delta U = (\varphi^T \varphi + R)^{-1} \varphi^T (R_s - FX(k_i)) \tag{14}$$

On the other hand, the matrix φ can help to obtain information of the material sensor regarding the thin film, which is subject to the air pressure. Moreover, the geometry (nanostructures) of the thin film can be stored over the matrix. Therefore, Equation (15) provides the correlation between the optimal predictive solution of the transduction with the matrix adaptive coefficients, which keep information of the material and geometrical characteristic of the designed sensor.

Furthermore, the periodical responses from the sensor/transducer are provided by Equation (15) though a transfer function analysis, thereby making it possible to identify the first order behavior in the steady state. Therefore, C_s represents the answer variable for the first order, N_s is the input excitation signal, t is the response time and K is the proportional gain.

$$\frac{C_s}{N_s} = \frac{K}{ts + 1} \tag{15}$$

Equation (15) is reduced in the time domain and Equation (16) is obtained, which keeps the model of Equation (5) in a steady state. In this context, the excitation signal is ΔP that looks for the response variable fluid flow Φ , and R is the constant derived from the first order solution for Equation (14) in Equation (10). Hence, it was possible to correlate stability parameters with the geometrical and material properties of the designed sensor.

$$\Phi = \left(\frac{\Delta P}{R} \right) \tag{16}$$

For this reason, the transducer adapts the signal received from the sensor according to the value measured of the physical variable to another equivalent (for example, the pressure difference transduced to its equivalent as an electrical signal, which is from “cmH2O” to “mV”). In this context, Figure 9 represents the static curve given in the section “A, B, C” for the coordinate system “X1, Y1”. However, the static curve can help to identify the linear response regions, by working in linear regions or with non-linear mathematical models.

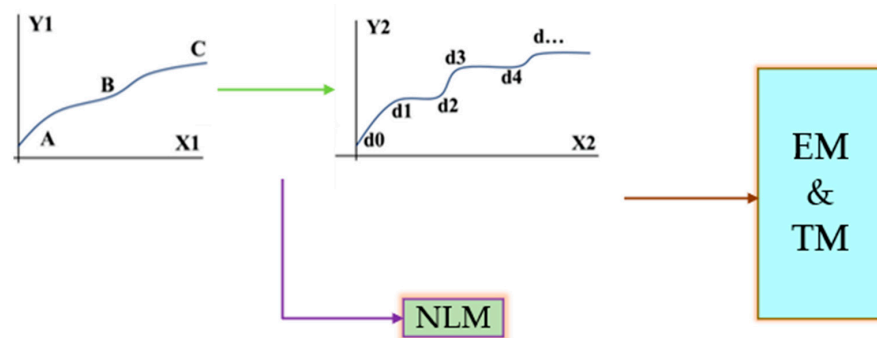


Figure 9. Scheme to represent the sensor/transducer data processing.

It should be noted that depending on the response time of the system (the system is considered as a research plant), it can lose information in the linearization process, due to its non-linear behavior, which is the reason why many authors suggest working in linear zones despite such risks (losing information in linearization process). In addition, the process of discretizing the signal information may also be lost, such as the dependence on the response time of the system and the sampling time (important parameter to discretize a signal).

Based on the conditions described in the previous paragraph, a transducer is necessary to transform the pressure difference into its electrical equivalent (in mV) in order to obtain the value for the air flow and also the displaced air volume. Theoretically, using Navier–Stokes models, the following relationship of the three physical variables is achieved: “pressure, flow and volume”, where the numerical solutions of the differential equations are also prone to loss of information as a dependence of the methodologies of numerical approximations in the solutions. However, the disadvantage of a completely theoretical

correlation is that the modeling of disturbances is frequently not achieved, which is solved by either approximation modeling or by correlation with experimental data.

Therefore, the transients of the plant’s dynamic system (while it is first-order) for the sections represented by $d_0, d_1; d_2, d_3; d_4, d \dots$ and with similar slopes only in the linear trends “AB” or “BC” are located in the coordinates “X2, Y2”. In such sections, the response times of the plant (the designed sensor/transducer) can be obtained.

Moreover, for each section, $d_1, d_2; d_3, d_4$, and “ $d \dots$ ”, henceforth the characteristics of overshoots, settling time, damping and parameters that indicate the stability of the designed system can be maintained.

The static and dynamic curves are algebraically interpreted as models of differential equations (polynomial models). Consequently, the correlation is obtained between the theoretical modelling and modelling based on the experimental data analysis results in the final model of the designed “sensor/transducer” system, that implies a response “Experimental Model (EM) and Theoretical Model (TM)” from linear (linearized) or completely non-linear (NLM) models.

Indeed, the system formed by the sensor/transducer represented by “ST” receives a mechanical signal “Ms1” (fluid mechanical signal for this case, which is pressure difference) and transforms it into the electrical equivalent “Es” or a response signal “Ms2” (fluid mechanics variable as volume or airflow equivalent signal). This conversion (transduction) requires characterization and calibration steps, which are depicted by the scheme summarized in Figure 10. From the static measurement data analysis, is possible to recognize the linear and nonlinear operations in the ST system. This information is quite important according to the design of the algorithm, which provides the final information of the ST measurement, such as the breathing variables of pressure, volume, and airflow.

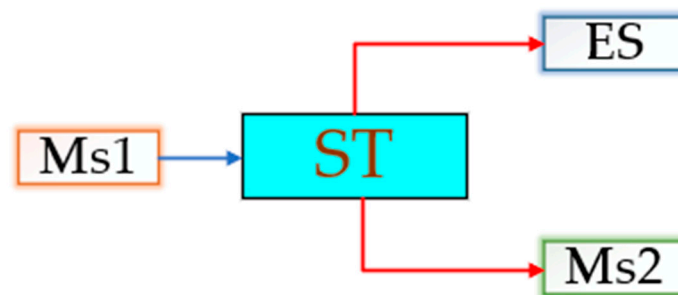


Figure 10. Scheme of a sensor/transducer system.

In the mathematical model of the sensor/transducer as a system, the transducer is composed by electronic devices that convert the fluid-mechanic variable of “pressure difference” to its electrical equivalent, as is the case for the variables “airflow and volume”. Furthermore, the characterization of each physical variable to be measured is necessary, with electro/mechanical devices that are able to measure the desired physical variables being monitored, which is showed in Figure 11.

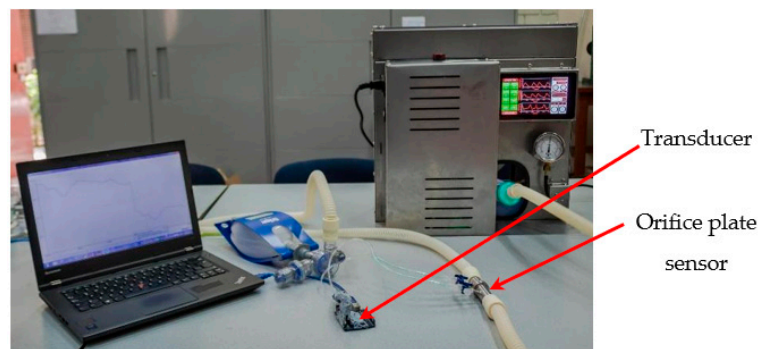


Figure 11. Setup of the designed sensor/transducer system.

3. Experimental Section

3.1. Orifice Plate Diameter Study

The working concept of the orifice plate is to generate a pressure difference which is related to the flow passing through it [1]. In this sense, different diameters could be considered; however, an optimum range of diameters presents a balance between the produced pressure difference sufficiently high to be used on the transduction stage, and sufficiently low to not to produce significant air flow or pressure drop in the breathing circuit.

Figure 12 (by views of subfigures a–c) shows the variable orifice-plate flow sensor it is manufactured by two pipes joined together with a ferrule clamp to have a quick release mechanism. Downstream of the ferrule clamp, an orifice-plate is welded to the flange. In this study, 5 parts were fabricated with different diameters: 4, 6, 8, 10, 12 mm. Distances of the pressure taps to the orifice plate were established according to the design considerations of an orifice plate air flow sensor [3]. However, the distance of the downstream pressure tap was not able to be less than half radius because of welding limitations for the geometry.

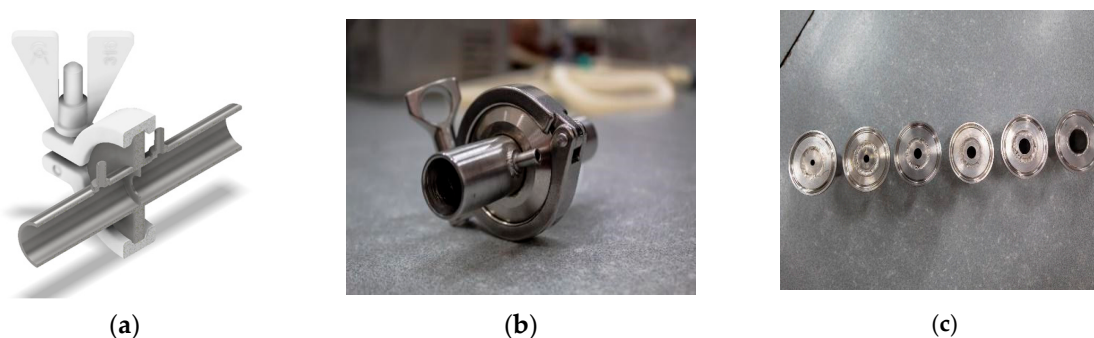


Figure 12. Variable Orifice-plate flow sensor.

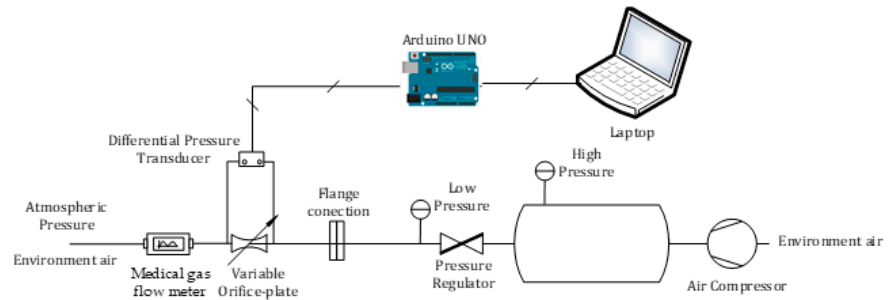
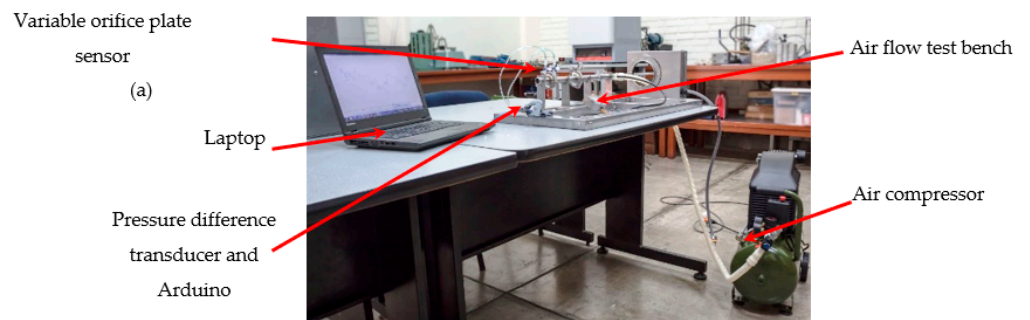
3.1.1. Steady State and Dynamic Response

The variable orifice plate air flow sensor was tested for the air flow measurement in a steady state condition. Figure 13a shows the experimental setup designed for this test, where the variable orifice plate was installed in the air flow test bench, an air compressor providing the air flow through the variable orifice plate sensor was included, a pressure difference transducer based on microphones connected to an Arduino UNO microcontroller board was integrated and an algorithm was designed and programmed for this transduction stage. Figure 13b shows a schematic representation of the experimental setup and the interaction of its components.

3.1.2. Measurement in a Mechanical Ventilator

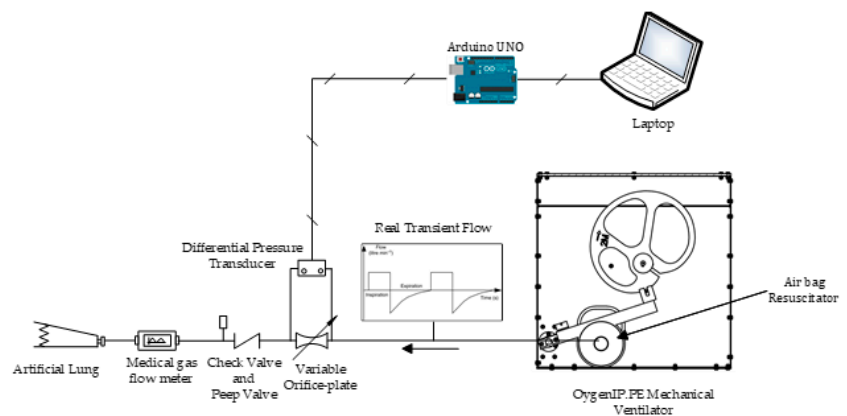
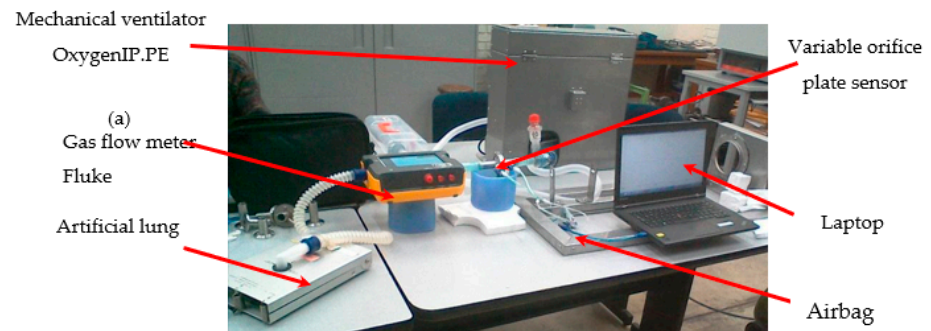
The variable orifice plate of the air flow sensor was installed in a breathing circuit connected to a mechanical ventilation system based on cams “OxygenIP.PE” [1]. This experiment corresponded to the real working conditions of the air flow sensor/transducer which was designed. A medical gas flow meter Fluke VT650 was connected to the circuit to obtain the real air flow over time, which is showed by the Figure 14a.

The artificial lung Fluke Accu Lung (a precision test lung) was used in order to simulate the ventilation parameters, which is showed by the Figure 14b as part of the experiments setup. This device is able to simulate 3 lung stages, from a healthy lung up to a damaged lung. A healthy lung corresponds to a compliance of 50 mL/cm H₂O and a resistance of 5 cm H₂O-s/L, while a damaged lung corresponds to a compliance of 10 mL/cm H₂O and a resistance of 50 cm H₂O-s/L. In this sense, for each orifice diameter inside the sensor, the experiment was run four times, twice for each lung parameters and twice for the minimum and maximum cams, XS and XL, respectively.



(b)

Figure 13. Schematic representation of experimental setup for steady state air flow.



(b)

Figure 14. Scheme of experimental setup for the sensor transducer connected to a Mechanical Ventilator.

3.2. Experimental Validation of the Sensor/Transducer Device

In the Figure 15, the designed sensor connected to the mechanical ventilator (Appendix A contains more details) is depicted; Figure 15a shows the designed sensor is shown to be connected to the air flow calibrator; and Figure 15b shows the air flow calibrator that needs to be connected to the personal computer in order to validate the expected measurements, and all the setup is showed by Figure 15c.

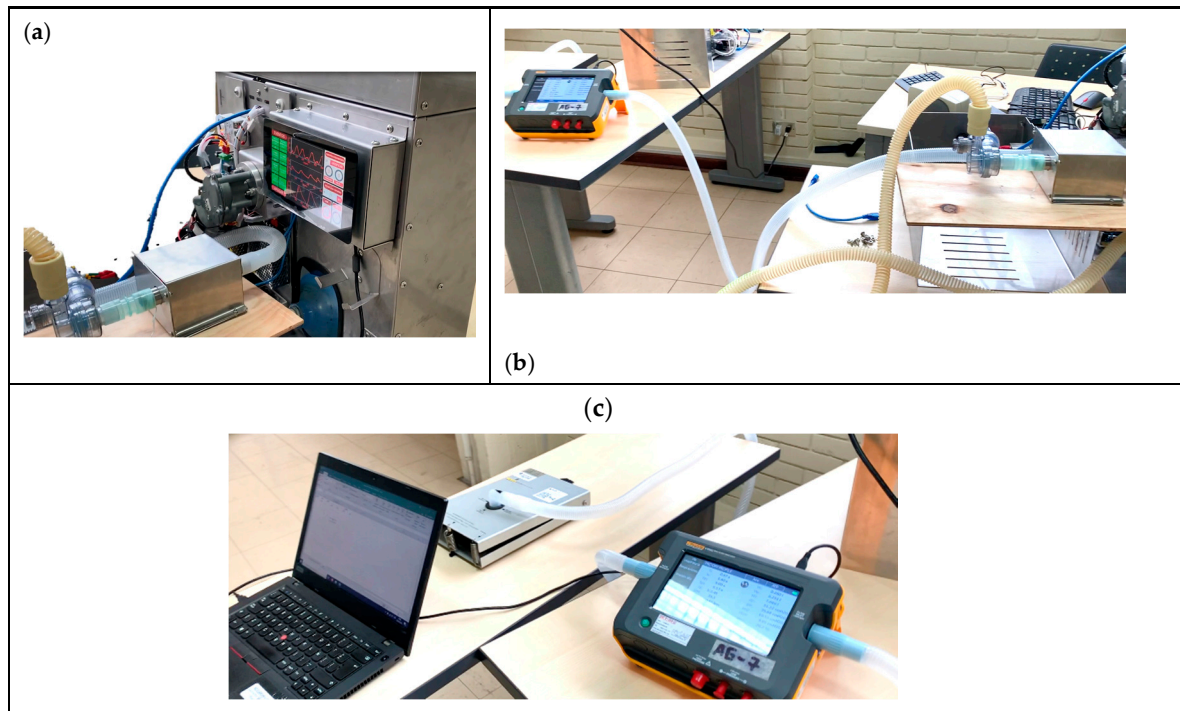


Figure 15. Setup of the sensor/transducer device connected to OxygenIP.PE Mechanical ventilator.

4. Results

4.1. CFD Simulation Results

4.1.1. Steady State Results

The following results were obtained for the steady state simulations for a 100 L/min airflow in a 10 mm diameter orifice. Figure 16a shows how the velocity increased as the area reduced (orifice throat), which is explained by the flow's intention of conserving the flow rate (mass conservation and incompressibility assumption). On the other hand, Figure 16b shows how the static pressure reduced, which occurred in response to the velocity's increase. This is explained by the flow's intention of conserving its momentum. It must also be noted that the behavior of these contours matched the results presented by Karthik [19].

4.1.2. Profile of Mechanical Ventilator Curves

A certain (expected) proportionality between the airflow and difference pressure curves is shown in Figure 17a. It is widely known that a higher pressure drop corresponds to a more abundant flow. This is explained because in turbulent flows the pressure loss is proportional to the flow velocity squared. This diameter alternative presents a maximum pressure drop of 274.28 Pa for a corresponding airflow of 67.74 L/min. Next, the steady and transient state analysis results were compared and plotted. Figure 17b shows an excellent similarity between the transient and steady state curves for the plotted points. Although a margin is observed between both curves, a good estimate of the transient behavior of the sensor can be modeled using steady state approximations. This behavior was expected,

since Funk et al. [20] concluded in their work that steady state approximations can be used in transient situations with excellent or valid results for most engineering applications.

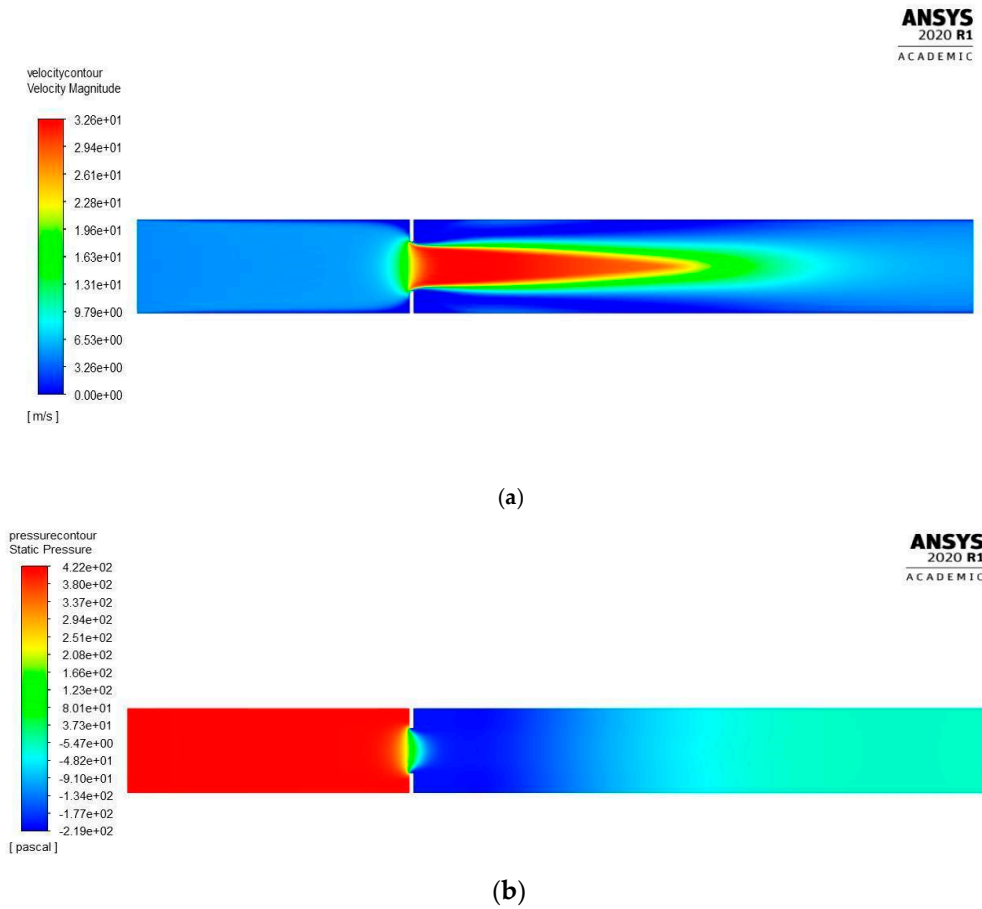


Figure 16. (a) Velocity Contours for a 100 L/min airflow, 10 mm diameter orifice; (b) Static pressure contours for a 100 L/min airflow, 10 mm diameter orifice.

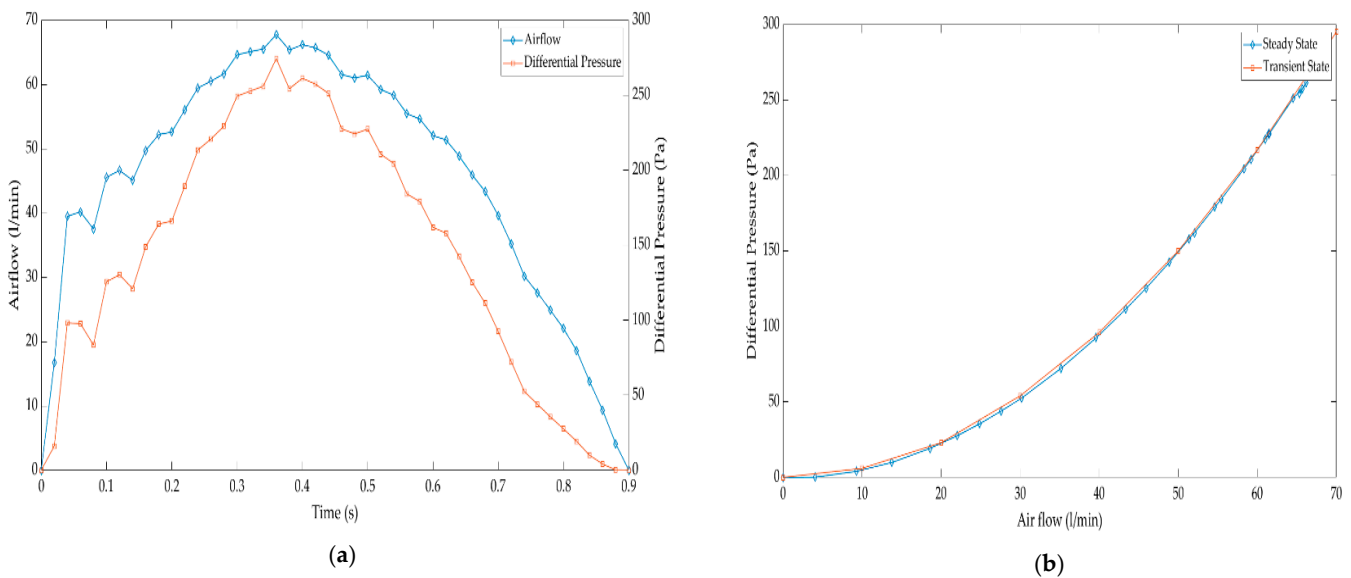


Figure 17. (a) Airflow profile and DP profile over time; (b) Steady vs. transient state results for a 10 mm diameter orifice.

4.2. Experimental Results

4.2.1. Steady State

In the following paragraphs, the results of experimental tests to verify the results of the proposed ST in steady state are provided. The analyses were made by comparisons with a Fluke instrumentation equipment, because the steady state information helped to obtain an understanding of the response of the designed ST under disturbances, such as unexpected overshoots or electromagnetic noise. In that context, the tests were run for the 4 mm diameter sensor/transducer and a steady-state inlet pressure of 5 mBar, 10 mBar and 20 mBar provided by an air compressor. A graphical comparison between the airflow plots is shown in Figure 18. The “Fluke” curve provides information of the airflow measured by the “Fluke” analyzer, and the “ST” curve shows the airflow as a response of the designed sensor/transducer ST.

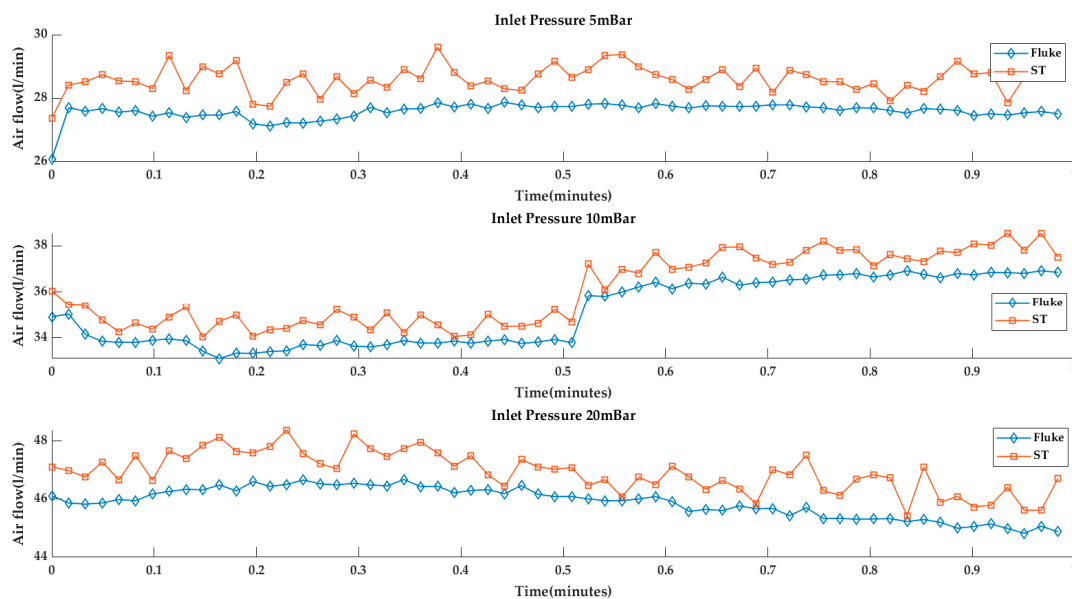


Figure 18. Flow and Flow ST for diameter 4 mm (Inlet pressure: 5, 10, 20 mBar).

The pressure difference curves (in mV) are plotted together in Figure 19. The “ST” curve provides information related to the pressure measured by the sensor/transducer in mV.

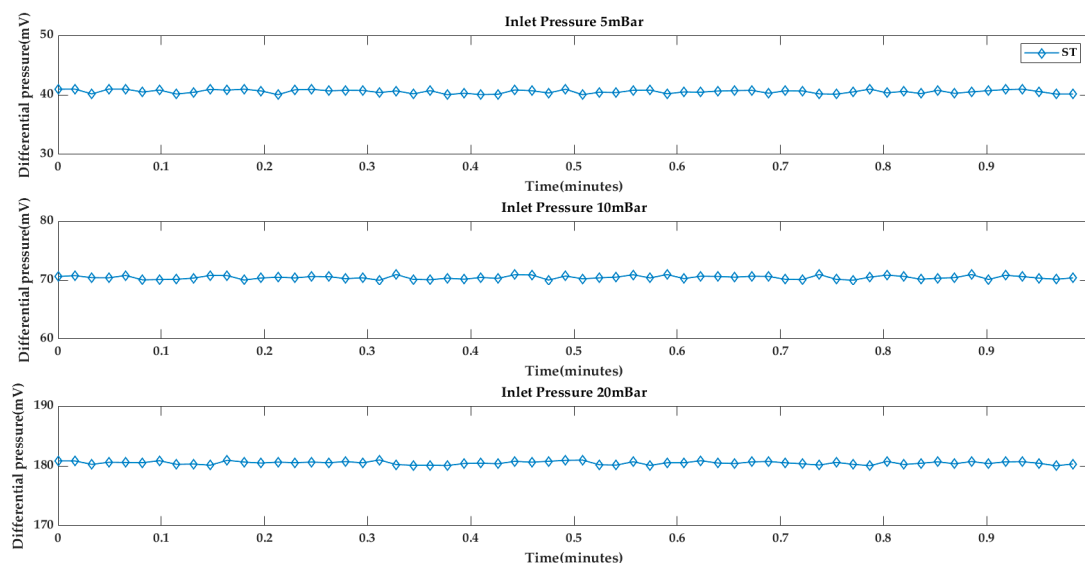


Figure 19. Pressure measured by ST in mV, for diameter 4 mm (Inlet pressure: 5, 10, 20 mBar).

The pressure difference curves are plotted together next in Figure 20. Each curve provides information of the pressure measured by the sensor/transducer in Pascal.

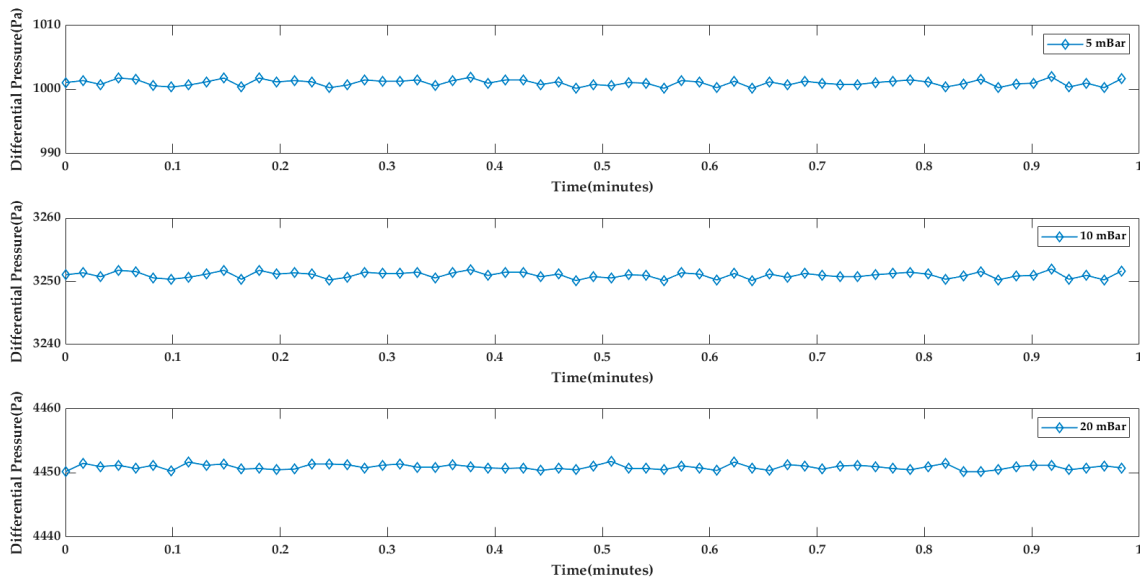


Figure 20. Pressure measured by ST (Pa), for diameter 4 mm (Inlet pressure: 5, 10, 20 mBar).

The tests were run for the 8 mm diameter sensor/transducer and a steady-state inlet pressure of 10 mBar, 20 mBar and 30 mBar was provided by an air compressor, for which the plotted airflow curves are shown in Figure 21. The “Fluke” curve provides information on the airflow measured by the “Fluke” analyzer, and the “ST” curve shows the airflow as the response of the designed sensor/transducer ST.

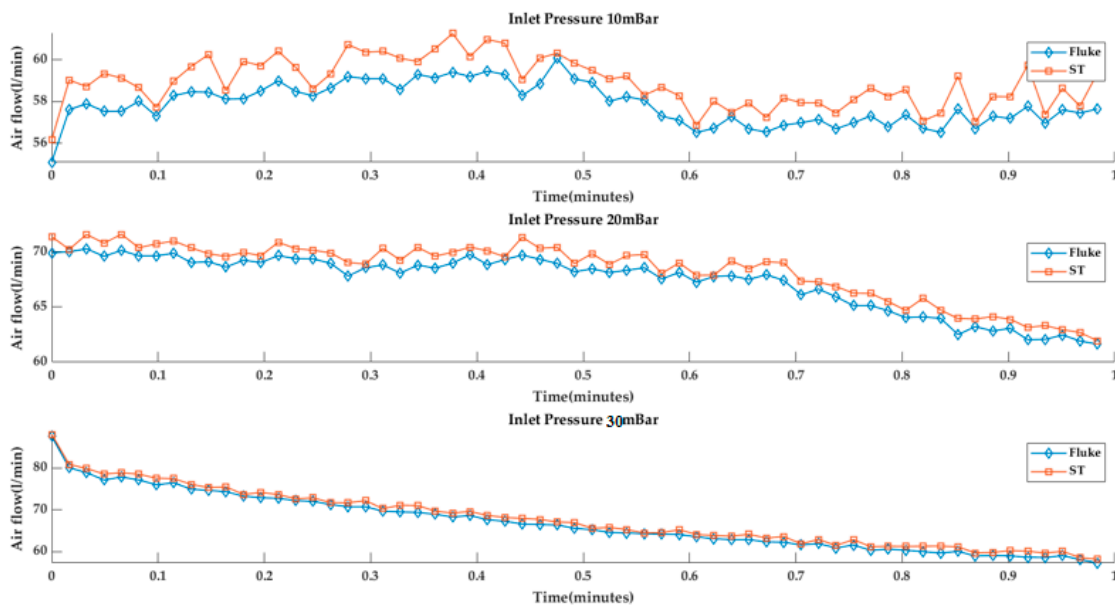


Figure 21. Flow and Flow ST for diameter 8 mm (Inlet pressure: 5, 10, 30 mBar).

The transduced pressure difference curves in mV are shown in Figure 22. Each curve provides information on the pressure measured by the sensor/transducer in mV.

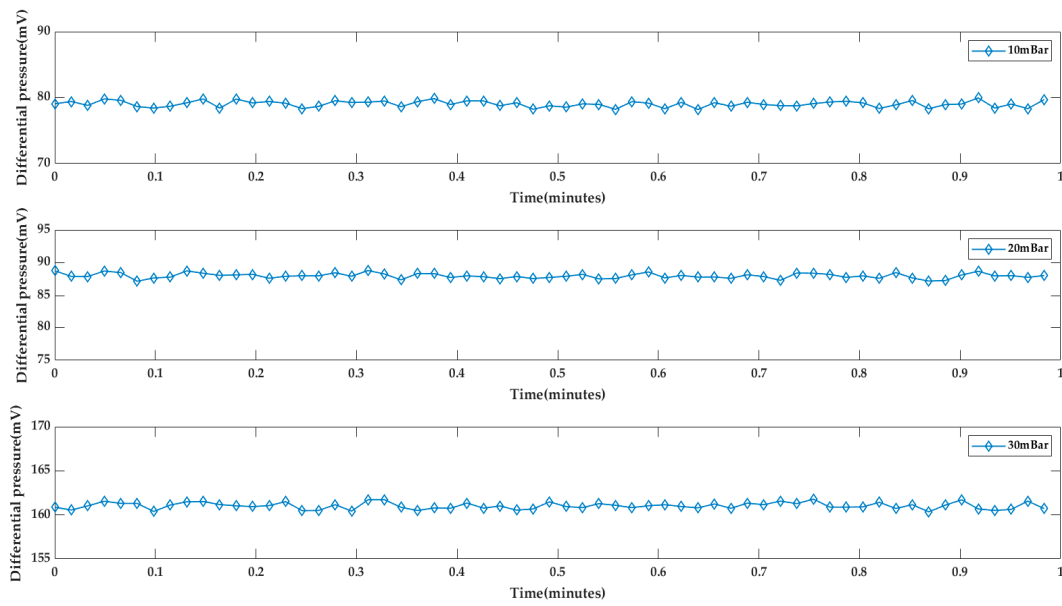


Figure 22. Pressure measured by ST (mV), for diameter 8 mm (Inlet pressure: 5, 10, 20 mBar).

On the other hand, the pressure difference curves are shown in Figure 23. Each curve provides information on the pressure measured by the sensor/transducer in Pascal.

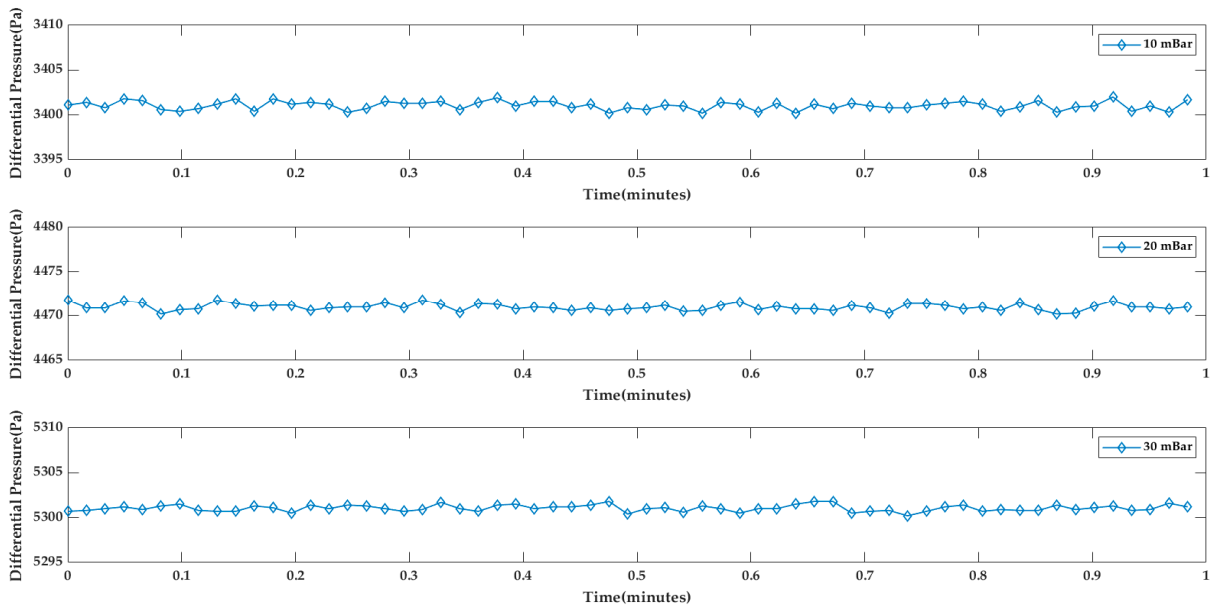


Figure 23. Pressure measured by ST (Pa), for diameter 8 mm (Inlet pressure: 5, 10, 20 mBar).

4.2.2. Open and Close Loop

Figure 24 shows the behavior of the airflow obtained by the designed sensor transducer (ST curve) in comparison with the airflow reference pattern (Fluke curve measured by the Fluke equipment). It is possible to understand that the ST system can measure changes in airflow when the tester prototype is closed or open to evaluate the steady state behavior of the designed ST. Nevertheless, it was possible to develop better responses of the system such as the dependence of the diameter of the ST, and the best responses (less error percent between ST and Fluke measurements) were achieved with orifice diameters of 8, 10 and 12 mm.

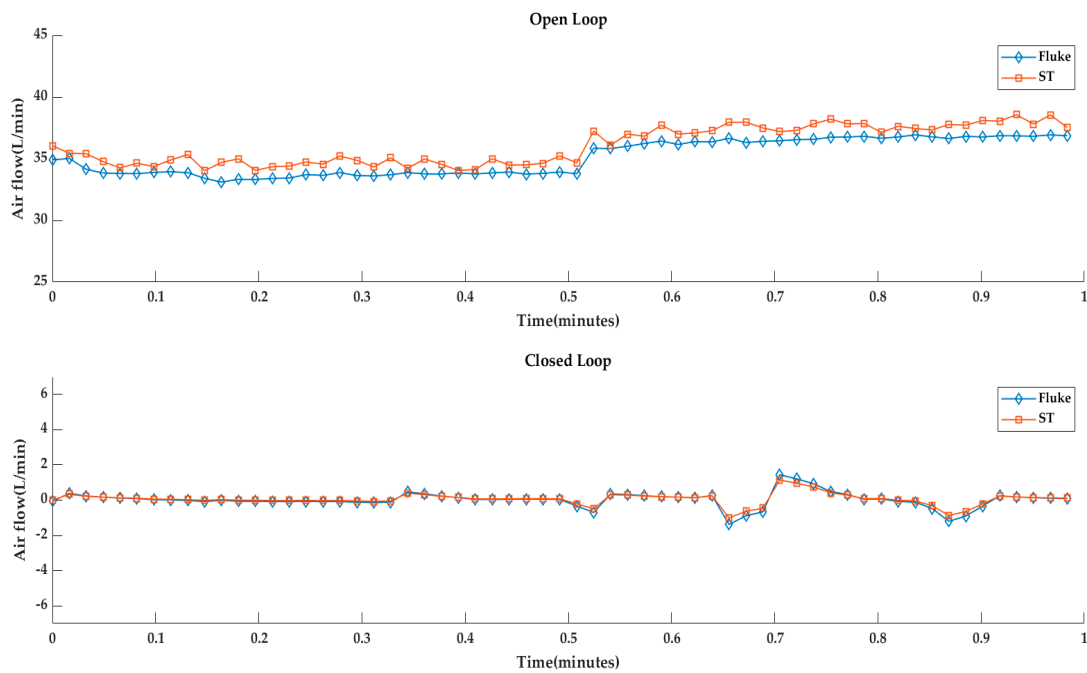


Figure 24. Airflow comparison in open loop and closed loop for the ST evaluation.

Figure 25 shows the pressure difference measured by the designed ST for a closed loop (upper subfigure) and open loop (lower subfigure). The ST system can detect changes or tendencies to maintain a steady state as a consequence of an open or closed loop of the tester prototype; therefore, it was possible to measure this pressure difference with the designed ST.

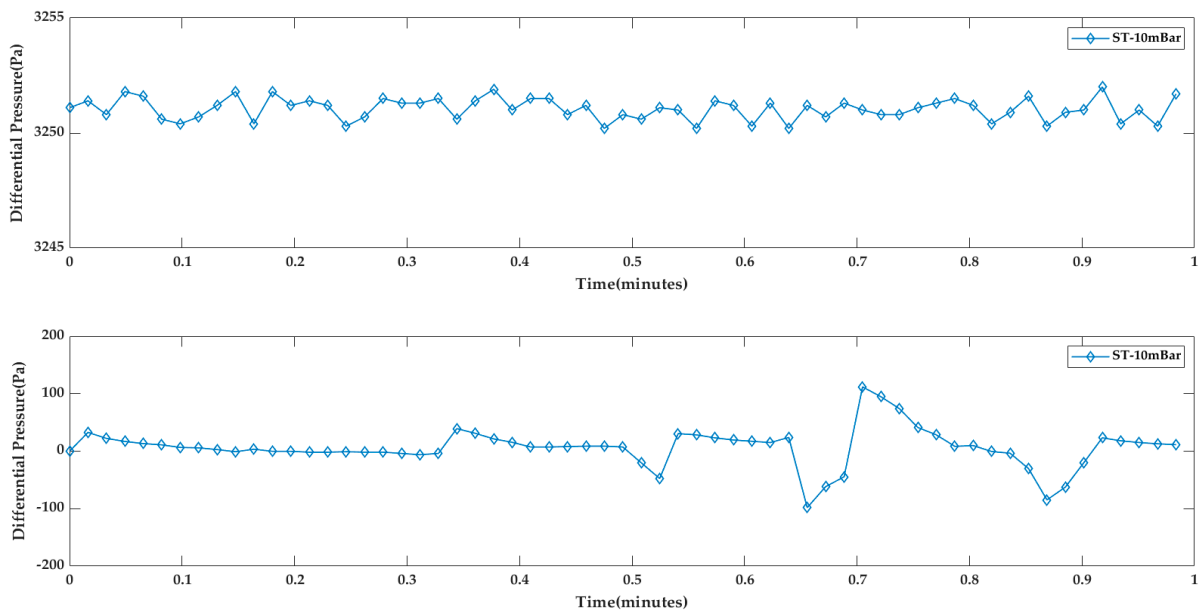


Figure 25. Pressure difference comparison in open loop and closed loop for the ST evaluation.

4.2.3. Dynamic Response

Figure 26 presents the dynamical response of the system ST to a pressure excitation signal given by 10, 20, 30 mBar obtained through the airflow regulated by the air compressor of the tester prototype, with an orifice diameter of 4 mm. It was found that ST cannot

provide a faster response in the presence of transient changes (red curves for airflow, pressure difference and volume).

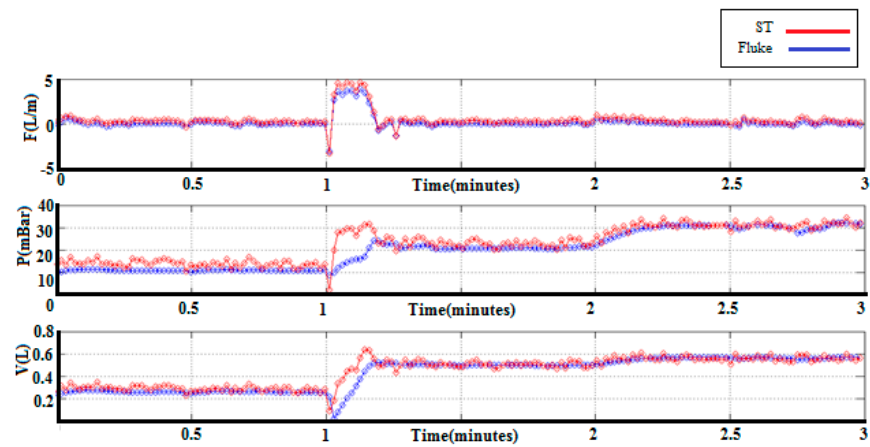


Figure 26. Flow, pressure difference and volume by dynamic analysis.

This can be explained by the geometrical characteristics of the ST and its nonlinear behavior in diameters from 4 mm to 6 mm; however, the ST system can provide a better response in the presence of disturbances or transient changes when the orifice diameter is between 8, 10 and 12 mm. The reference corresponds to the measurements of the Fluke equipment (blue curve for airflow, pressure difference and volume).

For the 8 mm diameter sensor/transducer and the mechanical ventilator excitation signals, the ventilation curves are shown in Figure 27. In every subfigure, the medical gas flow meter Fluke VT 650 proportionated the blue color curves in low frequency speed and red color for high frequency speed, which provide information on the volume, pressure and airflow (subfigures I–III), and the ST curves provide the volume, pressure, airflow the green color curves in low frequency speed and yellow color for high frequency speed (subfigures I–III). During the 2 min of measurement, the ST demonstrated a faster and robust sensor behavior (for 8 mm of diameter) as a consequence of the dynamical evaluation made by a low-cost mechanical ventilator based on cams OxygenIP.PE.

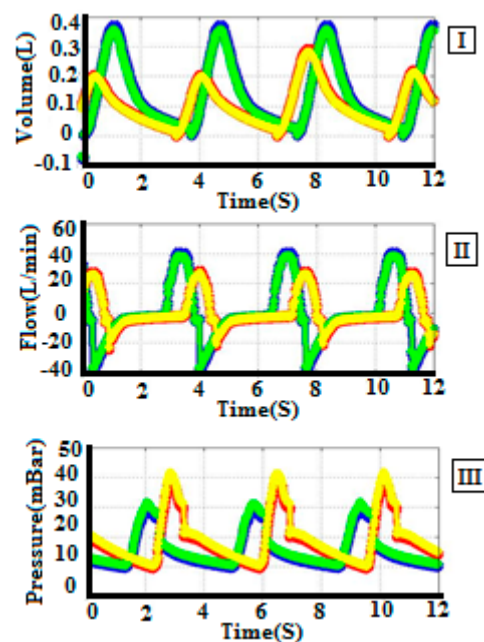


Figure 27. The dynamical behavior of the sensor/transducer connected to a mechanical ventilator low cost based on cams OxygenIP.PE.

Figure 28 shows the airflow curves for the 8 mm diameter sensor/transducer and the mechanical ventilator excitation signals. In every subfigure, the Fluke curves (blue color) provide information on the airflow measured by the medical gas flow meter Fluke VT 650 and the ST curves (red color) represent the airflow measured by the designed sensor/transducer.

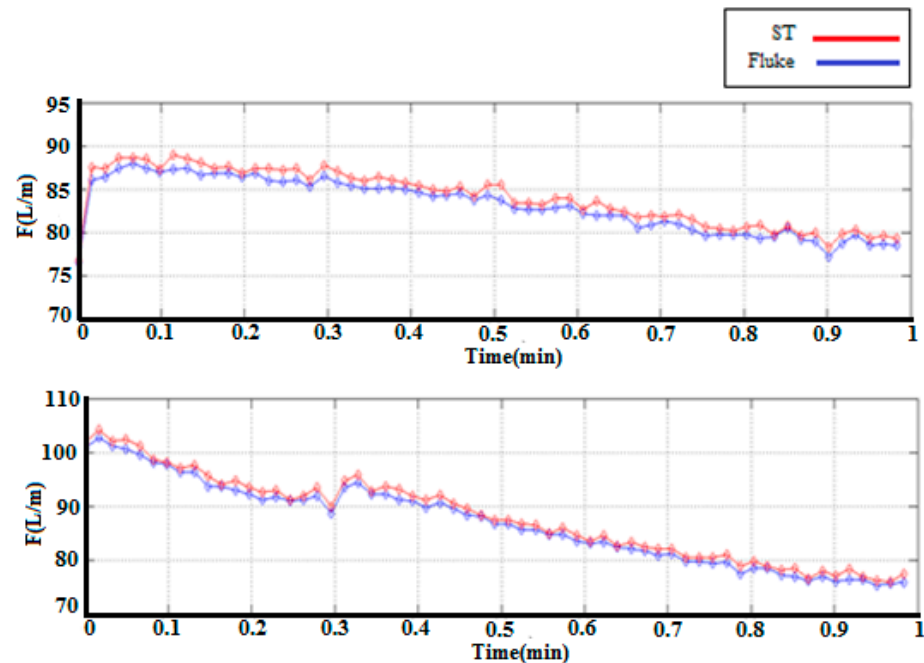


Figure 28. The dynamical behavior of the sensor/transducer connected to an air compressor in airflow range of work between 75 L/min and 105 L/min.

During the 1 min of measurement, the ST shows a faster and robust sensor behavior as a consequence of the dynamical evaluation made using an air compressor in the range of work from 75 L/min to 105 L/min.

5. Discussion

5.1. Data Interpretation Analysis

In order to interpret the experimental data with the designed algorithm, it was necessary to establish a correlation with the theoretical model to enhance the adaptive parameters of the polynomial model analyzed in Section 2.5.

Therefore, the experimental analysis of the designed polynomial model was correlated with Equation (18) in the theoretical model, as this equation gives the pressure difference “ΔP” as dependence on the airflow “Φ”, geometrical parameters “A₂, A₁” and flow density “ρ”.

$$\Delta P = \left(\frac{\Phi}{A_2}\right)^2 \left(\frac{\rho}{2}\right) \left(1 - \left(\frac{A_2}{A_1}\right)^2\right) \tag{17}$$

The theoretical model only produces a quadratic relationship between the airflow with the pressure difference, while “A₂” tends to decrease, the pressure difference and airflow tend to increase.

Since the airflow for the breathing analysis had an “increasing and decreasing behavior”, to obtain an appropriate measurement with the designed ST, the static and dynamic behavior of the sensor was studied using an adaptive analysis of the polynomial model.

Therefore, the static behavior was provided as a dependence of “airflow, pressure difference, and diameter”. Figure 29 depicts a flow and two points crossing its axis, for which P₁, V₁, Y₁ and P₂, V₂, Y₂ are the pressure, flow speed, and position at points 1 and 2, respectively.

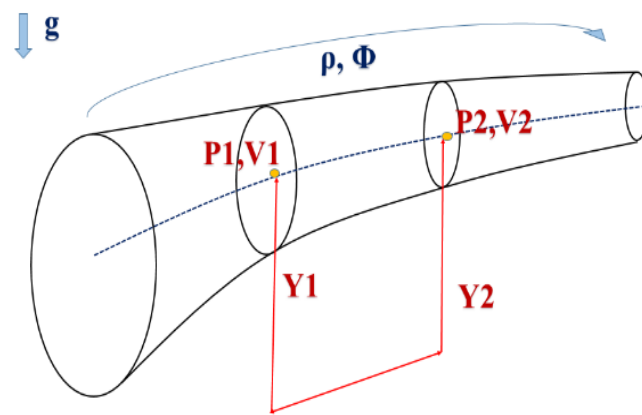


Figure 29. Schematic representation of airflow transmission through points 1 and 2.

The static curve gives the relation among two variables in order to identify a linear and nonlinear range of work; therefore, it is possible to understand its dynamic behavior.

The dynamical analysis of the airflow attempts to obtain the linear answer of the system so that the ST can make estimations of the physical variables volume, and pressure as a consequence of the pressure difference, which was achieved by the correlation between the experimental and theoretical analyses described in previous chapters. Therefore, the curves “A, B, and C” represent the airflow curves that were expected to be achieved in the characterization of the interpretation data with the ST, which is depicted by the Figure 30.

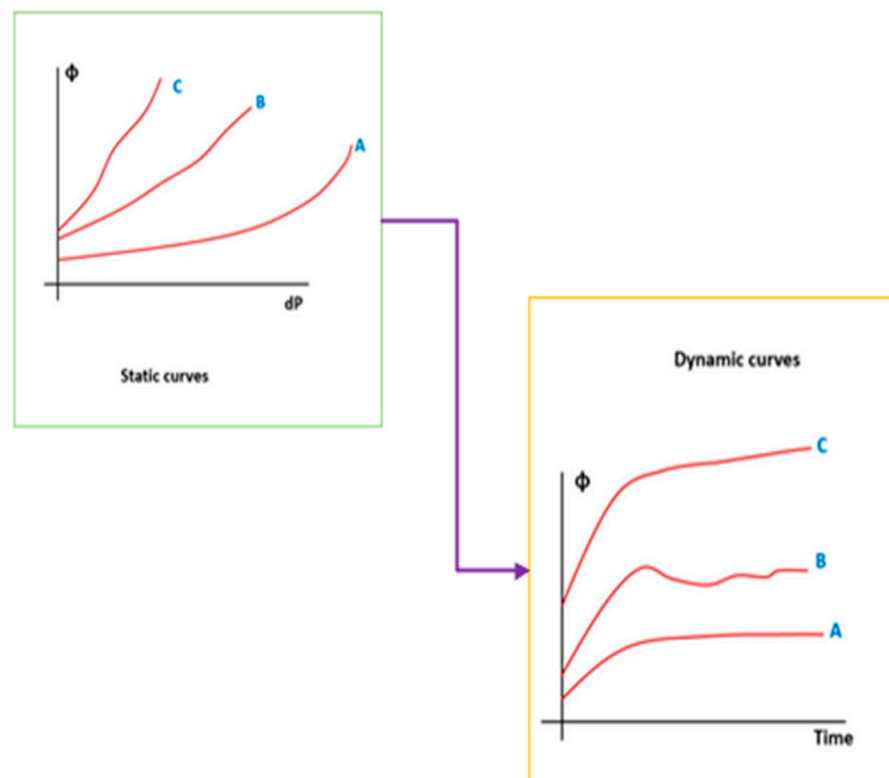


Figure 30. Schematic representation of the airflow dynamic and static behavior.

Two types of studies were performed, one for the static responses of the ST system, and another for the dynamic ones. The first was conducted using a tester prototype with a compressor as an air source, which is depicted in Figure 31 and was used for the static and dynamic tests. The pressure difference measured by the sensor was calibrated in order to provide the same response as the air flow meter Fluke. Finally, the other group of static

and dynamic tests was performed with the mechanical ventilator as the air source. Hence, the pressure difference registered provided information to understand the dynamics of the breathing variables (pressure, volume and airflow) in order to understand the behavior of the sensor/transducer as part of the ventilation circuit.

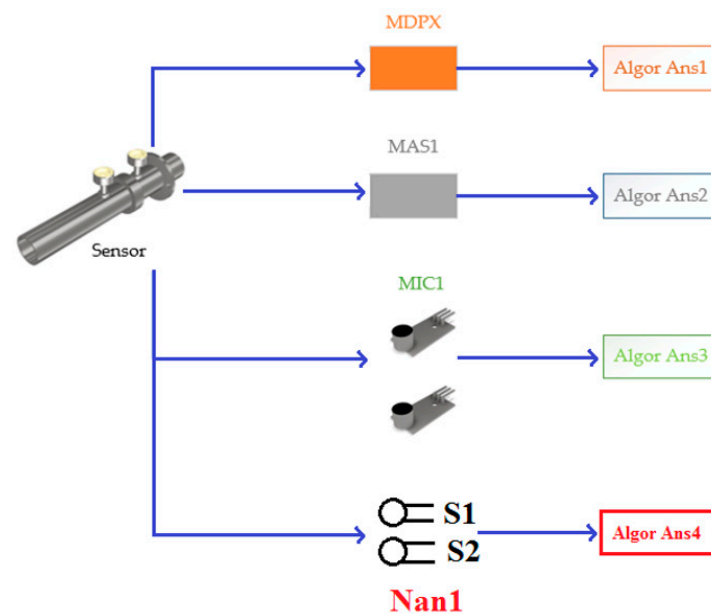


Figure 31. Block diagram testing transducers.

The designed ST depends on the diameter and pressure difference; for this reason, it was necessary to choose which transducer to use to obtain the electrical equivalent of the pressure difference. Finally, the evaluated alternatives were as follows: transducer MAS1, the integrated circuit MDPDX10P, the transducer constructed with two small microphones sourced from the ARDUINO company, and a transducer based on nanostructures. Different alternatives are shown in Figure 31.

The measured pressure difference by the designed ST was central to obtaining the airflow after a transduction process, which was obtained by MDPX and MAS1, making the electrical equivalent conversion from air pressure difference signal to airflow signal in Volts. The electrical transduction was performed with two microphones measuring decibels and correlating with pressure by converting the response to volts. The electrical equivalence values help to analyze the statistics of the physical variables “air pressure, volume and airflow” as a consequence of the designed algorithms by polynomial (as they are depicted by “Algor Ans1”, “Algor Ans2”, and “Algor Ans3” in Figure 31) correlations between the transduction signals. However, in order to enhance the robustness and response time of the designed ST, we modified the samples that receive the pressure difference by samples based on nanostructures of AAO, as is depicted in S1, S2 in Figure 31, which also send the transduction information through the algorithm depicted by “Algor Ans4”.

The best estimation of the breathing physical variables “airflow, pressure, and volume” was chosen because of the pressure difference transduction techniques that were studied in the previous chapters. These microphone-based transducers obtained estimated variables with a maximum error of 1% in a steady state, while the MAS1-based transducer estimated variables with a 0.95% error in a steady state. In turn, the MDPX-based transducer presented a steady-state error of around 2%. However, the cost of the microphone-based transducer was around 70% cheaper than the most expensive transducer, the MAS1. For this reason, the microphone-based transducer was selected as the main transducer for the designed ST.

When performing the main analysis of the transducer algorithm, we sought to identify the adaptive coefficients from the experimental data obtained by the transducer and the polynomial identification estimate using pressure difference “DP”, the pressure “P”, the

airflow “F”, and the volume “V”. If the adaptive estimation was predicted according to the reference variable with an error of less than 1% in the steady state, then the ST provided information on the breathing variables, which is depicted in Figure 32.

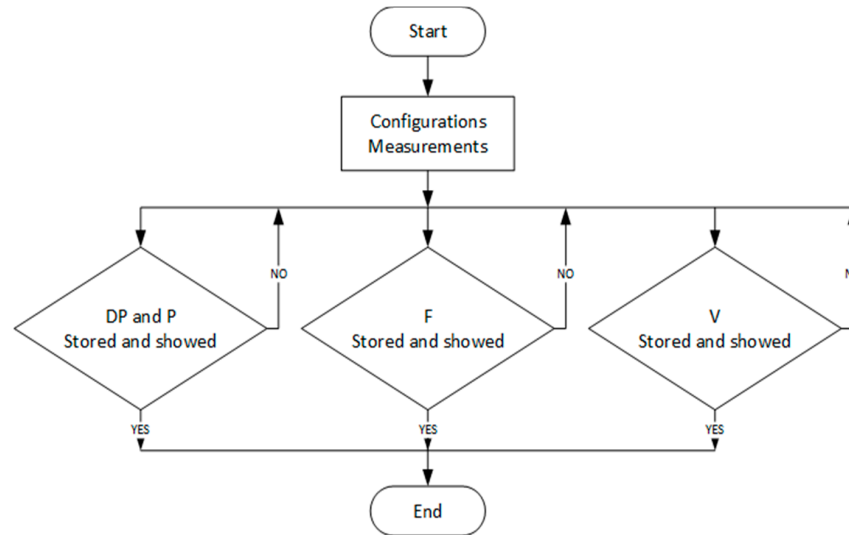


Figure 32. Flow diagram of the ST measurement and data storing.

Therefore, it was necessary to define the input variables in order to correlate the estimated responses under the dependencies of the references variable. Figure 33 shows the two input variables of the system from the data interpretation analysis, which are given by the pivot displacement in sexagesimal degrees (red curve color curve in subfigure III of Figure 33). The pressure difference in its electrical equivalent (mV) was considered as a second input or excitation variable (blue color curve in subfigure I of Figure 33). Moreover, the pressure difference measured by the nanosensor based on nanostructures, as shown in subfigure II, revealed that the nanostructure sensor maintains a rapid response time and robustness under disturbances of the pivot (green color curve in subfigure II of Figure 33).

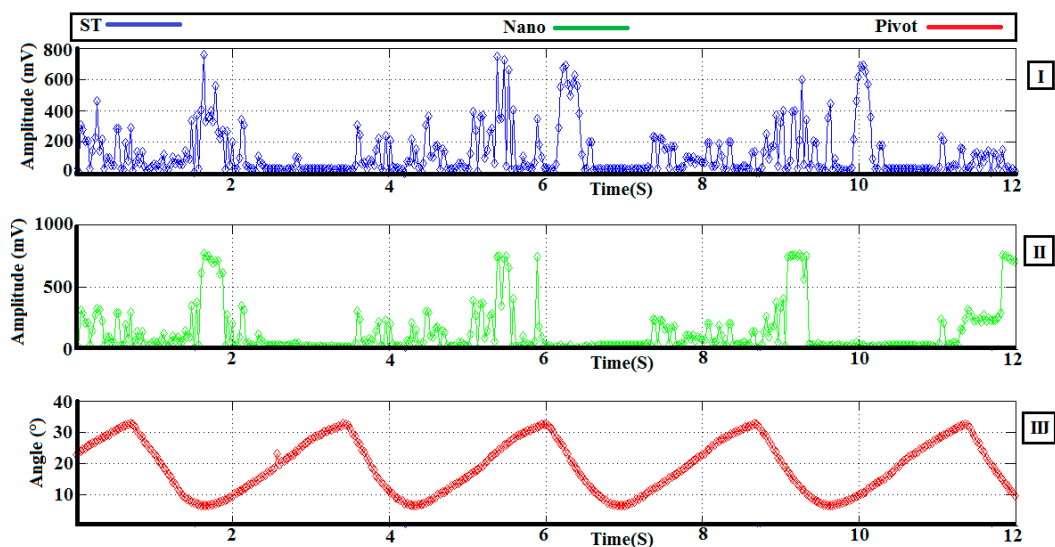


Figure 33. Motor angle displacement and microphones answer.

As a consequence of the input excitation signals, it was possible to achieve and identify the adaptive coefficients which were evaluated in high and low operation because the frequency range of the requirements is between 15 Hz and 20 Hz.

Therefore, Figure 34 shows the result of the ST as a consequence of the electrical transduction from the pressure difference to the airflow values in millivolts for cams of extra small, medium, and extra-large sizes. The obtained data are presented in Figure 34 in subfigures I–III, in which blue indicates high frequency and red curves low frequency.

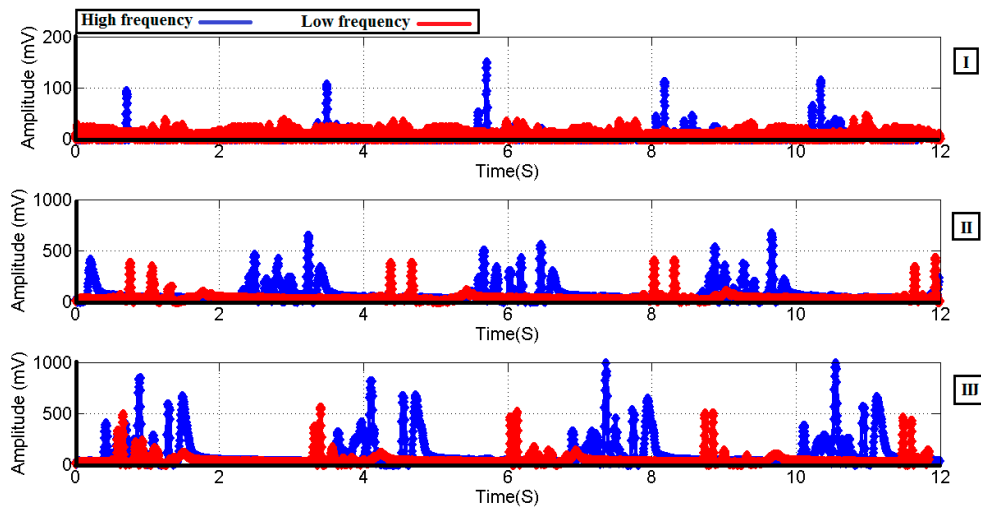


Figure 34. Microphones in high and low operation.

On the other hand, it is apparent that for the ST response as a consequence of the electrical transduction from the pressure difference to the airflow values in millivolts for cams of extra small, medium, and extra-large sizes, the information achieved is shown in Figure 34 for the subfigures I–III, in which the blue color indicates high frequency and red represents low frequency. With this information, it is possible to identify a linear range of work.

The ventilator works as an intermediary for the signal received from the rotor position sensor (RS1(AS5047) and RS2) used to measure the rotor speed of the motor and control it with a driver (DR1) that has its own control system with its own actuator and sensor with an electrical current to the motor (M).

This is the reason why a controller (as central control unit) also requires the signal from a rotor position sensor to measure the angular displacement of the pivot to provide an estimation of the air volume, and finally, the airflow sensor (FS1), which has its own transduction algorithm to provide information to medical doctors through the touchscreen panel, as depicted in Figure 35.

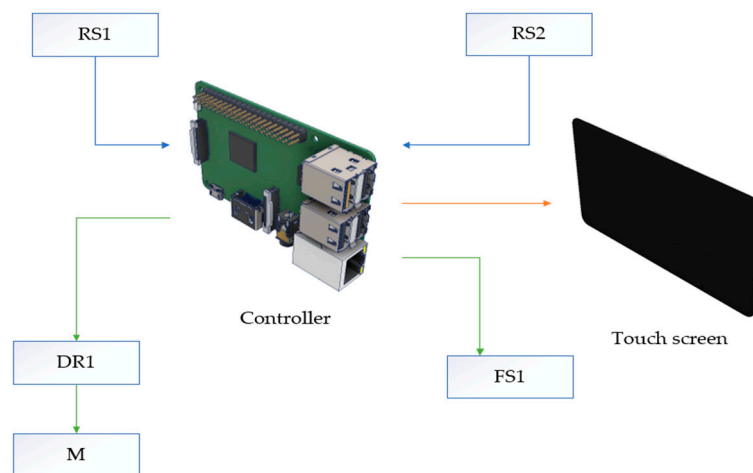


Figure 35. Block diagram of the control system for online operation.

The ST achieved good performance for the diameter of 8 mm due to its optimal response based on appropriated magnitudes and tracking for the mechanical ventilator curves. In the “data interpretation analysis” the ST with an orifice diameter of 10 mm was used. Despite the nonlinear response, the airflow was obtained because of the good performance of the ST algorithm in transducing the pressure difference signal to the airflow variable for a larger range of work (low and high speed of the ventilator).

The range of work of the test was limited to a high frequency of 20 Hz and a low frequency of 15 Hz. The transduction was achieved with the microphone sensors used to obtain the pressure difference as is shown in Figure 36I, where the blue curve provides information about the system working at high speeds and the red curve for low-speed operation. Figure 36I shows that at high speeds it was possible to obtain an increased amplitude (50 percent). Both signals were achieved in millivolts due to the transducer (small microphones) having greater sensitivity at higher speeds.

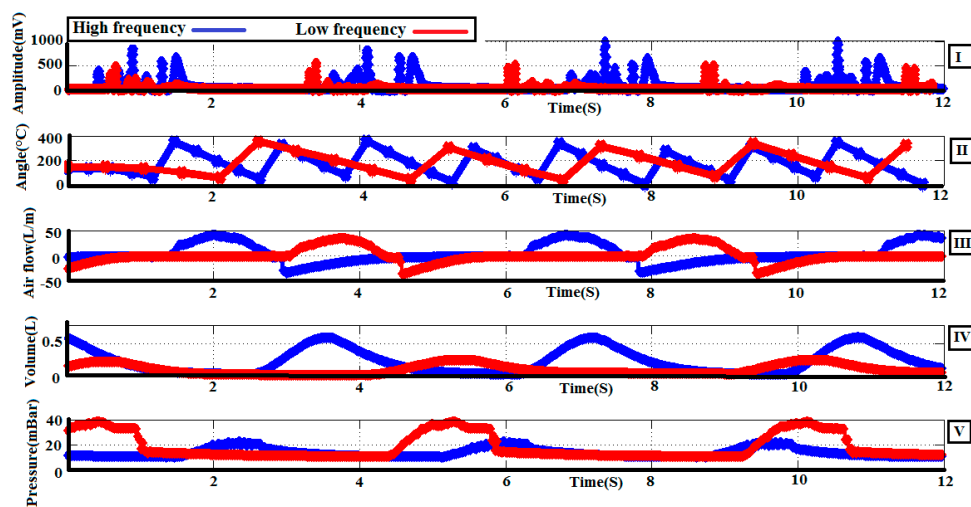


Figure 36. Microphones answer in high and low operation and small and big cam.

Furthermore, it was necessary to define the input variables to correlate the estimated responses under the dependencies of the reference variable (analyzed in previous chapters). Figure 36II shows the input variables of the system from the data interpretation analysis, which are given by the motor displacement in sexagesimal degrees, with the blue curve indicating high speed and red curve representing low speed. It is necessary to remember that motor displacement causes pivot displacement and it is enough to use only one sensor to achieve the angle displacement during the polynomial correlation variable analysis.

Therefore, the main variable obtained from the ST is the airflow rate, given by the transduction operation supported by the predictive estimations for the other breathing variables “volume and pressure” obtained by the polynomial analysis (described in chapters lines above) from the airflow variable.

Figure 36III–V presents the airflow rate, volume, and pressure, respectively, in which the blue color curves are the airflow, volume, and pressure in high-frequency operation, and the red color curves are the airflow, volume, and pressure in low-frequency operation, which were obtained as a consequence of the predictive/adaptive algorithm; however, it is necessary to keep in mind the importance of the previous data analysis during the characterization and calibration of the ST to obtain the presented results.

It was necessary to develop a multivariable control algorithm to control the respiratory variables (air flow, pressure and volume), hence the pressure difference transduced in volume, air flow and pressure as respiratory variables required a multivariable control algorithm, which was able to control the rotor speed of the mechanical ventilator motor, the air pressure difference and the air flow, as the implicit function, pressure and volume.

5.2. Rotor Speed Control of the Mechanical Ventilator Motor

The rotor speed control of the mechanical ventilator motor was achieved by an adaptive predictive model, for which a system identification of the motor physical parameters was necessary. However, unexpected disturbances caused by vibrations during the cam movement can reduce the performance of the control. Therefore, it was necessary to design a PID (Proportional, Integral and Derivative) control as part of the identification system to achieve the physical parameters of the mechanical ventilator motor.

Hence, the control inside the identification of the motor parameters was obtained by the classic PID controller equation in the Laplace (S) domain, in which KP_p is the proportional constant, KI_p is the integral constant, and KD_p is the derivative constant.

$$PID(S) = KP_p + \frac{KI_p}{S} + KD_p S \tag{18}$$

The plant (mechanical ventilator motor) was analyzed in two sections, namely the electrical section and the mechanical section which are described in the following paragraphs.

Rotor Control Position of the Mechanical Ventilator Motor as a Function of Electrical Current

The rotor control position of the mechanical ventilator motor is depicted by the block diagrams in Figure 37. $Inp(S)$ is the electrical current signal as the input excitation signal, $Yans(s)$ is the position response that is necessary to obtain the speed of the motor, $Cont(S)$ is the controller during the identification system, $Plant(S)$ is the transfer function for the plant that is the electrical motor composed by its electrical subsystem and its mechanical subsystem, and $Sens(S)$ is the transfer function for the position sensor.

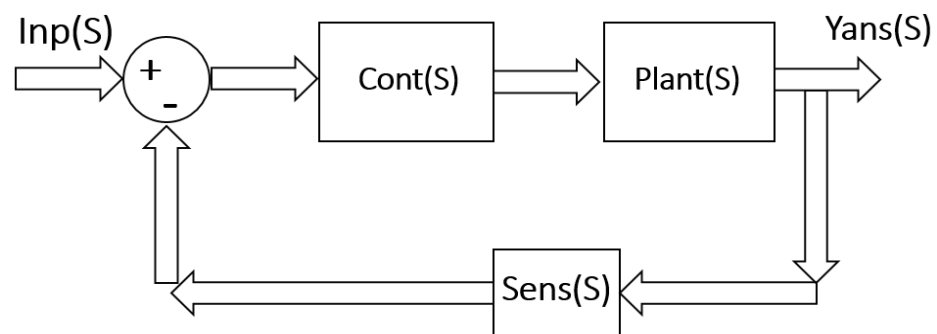


Figure 37. Block diagram for the rotor position control of the mechanical ventilator.

Using the algebra analysis from the block diagram depicted above, the following is obtained:

$$Inp(S) - Sens(S)Y(S)Cont(S)MS(S) = Y(S) \tag{19}$$

From which following equation is achieved:

$$\frac{Yans(S)}{Inp(S)} = \frac{Cont(S)Plant(S)}{1 + Cont(S)Plant(S)Sens(S)} \tag{20}$$

In Equation (20), the transfer function for the rotor position sensor is generalized, but in spite of that, the response time of the position sensor is very short in comparison to the speed of the motor. Hence, its transfer function was reduced as $Sens(S) = Ks$. Therefore, the characteristic equation is given by Equation (21), in which m is the mass of the rotor motor, k_i is the electrical current coefficient of the motor and k_y is the displacement coefficient of the motor.

$$\left(KP_p + \frac{KI_p}{S} + KD_p S \right) \left(\frac{K_i}{m S^2 + K_y} \right) Ks + 1 = 0 \tag{21}$$

The reduction of the equation above is given by Equation (22).

$$\left(KD_p S^2 + KP_p S + KI_p \right) K_i K_s + S(mS^2 + K_y) = 0 \tag{22}$$

Equation (22) is organized in Equation (23) as a polynomial in descending order.

$$S^3 + \frac{(KD_p K_i K_s)}{m} S^2 + \frac{(KP_p K_i K_s + K_y)}{m} S + \frac{KI_p K_i K_s}{m} = 0 \tag{23}$$

The controller’s parameters need to be obtained by different methodologies such as a stability analysis and a comparison with the theoretical model of dynamic systems given by Equation (24) [21], in which ω_0 is the natural frequency for the system, ϵ is the damping effect, and α is the coefficient as the auxiliary connector between Equations (23) and (24).

$$S^3 + \omega_0(2\epsilon + \alpha)S^2 + \omega_0^2(1 + 2\epsilon\alpha)S + \alpha \omega_0^3 = 0 \tag{24}$$

Therefore, the controller parameters KP_p and KI_p , can be obtained by the comparison of the coefficients from Equations (23) and (24), from which Equations (25)–(27) are proposed as functions of K_i , K_s , KD_p , m , ω_0 and ϵ .

$$\frac{(KD_p K_i K_s)}{m} = \omega_0(2\epsilon + \alpha) \tag{25}$$

$$\frac{(KP_p K_i K_s + K_y)}{m} = \omega_0^2(1 + 2\epsilon\alpha) \tag{26}$$

$$\frac{KI_p K_i K_s}{m} = \alpha \omega_0^3 \tag{27}$$

Moreover, α is obtained from Equation (27) and represented by Equation (28)

$$\alpha = \frac{KI_p K_i K_s}{m\omega_0^3} \tag{28}$$

The controller parameter KI_p is obtained by analyzing Equations (25)–(28), and presented in Equation (29)

$$KI_p = KD_p \omega_0^2 - \frac{2\epsilon m \omega_0^3}{K_i K_s} \tag{29}$$

In a similar context, the controller parameter KP_p is obtained with Equations (25)–(29), and presented in Equation (30).

$$KP_p = \frac{2\epsilon K_i K_s KD_p \omega_0 + m \omega_0^2 (1 - 4\epsilon^2) - K_y}{K_i K_s} \tag{30}$$

Therefore, Equations (29) and (30) are the integral and proportional controller parameters that determine the controller parameter KD_p , which can be analyzed as a reference parameter (analyzed by stability of the dynamic system) to find the PID control for the motor of the mechanical ventilator. However, the identification parameters of the motor require a controller with slow reactions to provide sufficient time to identify the parameters of the system, and the controller selected for the identification of the physical parameters of the mechanical ventilator motor was a PI controller, hence the derivative parameter KD_p becomes null, and Equation (30) can be obtained from Equation (29), thereby providing the integral parameter of the PI controller.

$$KI_p = -\frac{2\epsilon m \omega_0^3}{K_i K_s} \tag{31}$$

Finally, Equation (32) is the proportional parameter of the PI controller obtained from Equation (30) when the derivative parameter is null.

$$KP_p = \frac{m\omega_0^2(1 - 4\epsilon^2) - K_y}{K_i K_s} \tag{32}$$

5.3. Model Predictive Control Analysis

While the above results indicate good control, they lack a fast response which could be obtained using a predictive model, such as an Optimal Predictive Control model described in more detail in the following (Appendix B).

The optimal excitation signal in order to find the optimal response is given by [1,13]

$$\Delta S = (\phi^T \phi + A)^{-1} \phi^T (A_S - LX(k_i)) \tag{33}$$

Therefore, using the last equation, the optimal control response for the pressure difference can be achieved, as well as the rotor speed and implicitly the volume, airflow and pressure. Moreover, the optimal response control can be enhanced by the specific weight matrix “W” that must be included in Equation (A5). Equation (33) has similarities with Equation (A9) but the difference is given by the adaptive matrix coefficient “ϕ”, because for this analysis the matrix depends only on the requirement control strategies while maintaining its dependence on “ϕ” (the geometrical and material coefficients of the designed ST).

As a consequence, the main control algorithm was designed using the adaptive cascade model, which is depicted in Figure 38 in which “U1” is the input variable (pressure difference measured by the designed ST) and the internal response variable is the air flow “U2”, which is the input variable used to obtain the pressure “Y1” and volume “Y2”, moreover the internal control variable of the rotor speed has a correlation with the desired airflow required by the mechanical ventilator.

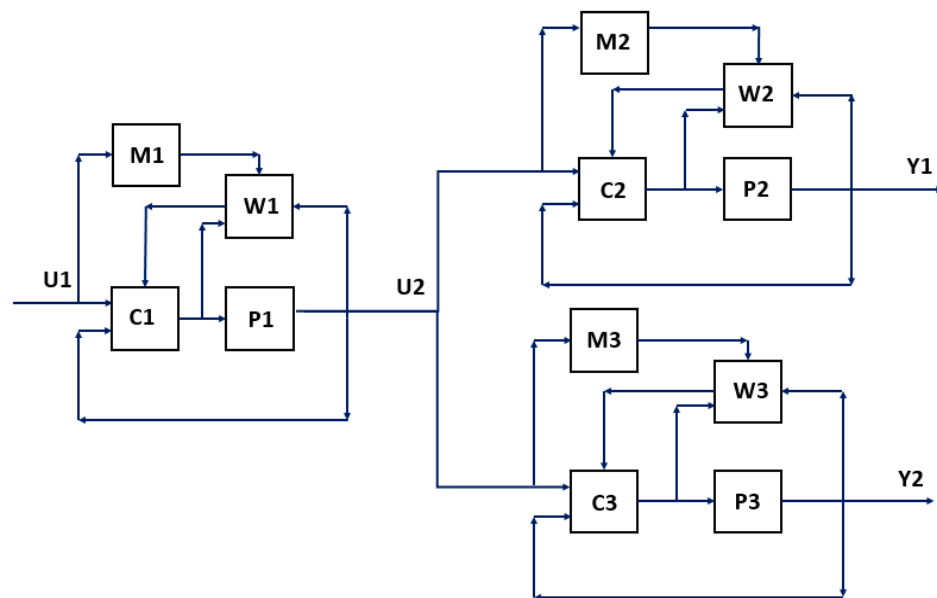


Figure 38. Control adaptive cascade model for the ventilator control system.

To evaluate the performance of the designed ST in comparison with its enhancement based on AAO nanostructures, experiments of the mechanical ventilator controlled by the adaptive cascade algorithm in Huancayo (3250 m over sea level) were conducted. It can be seen in Figure 39I that the curves as well as the controlled air flow (implicit) measured by the designed ST (blue colour curve) and the air flow measured by the designed ST

enhanced by nanostructures (red colour curve) were obtained with a steady state error of 1.4% of the ST and 0.8% for the ST enhanced by nanostructures.

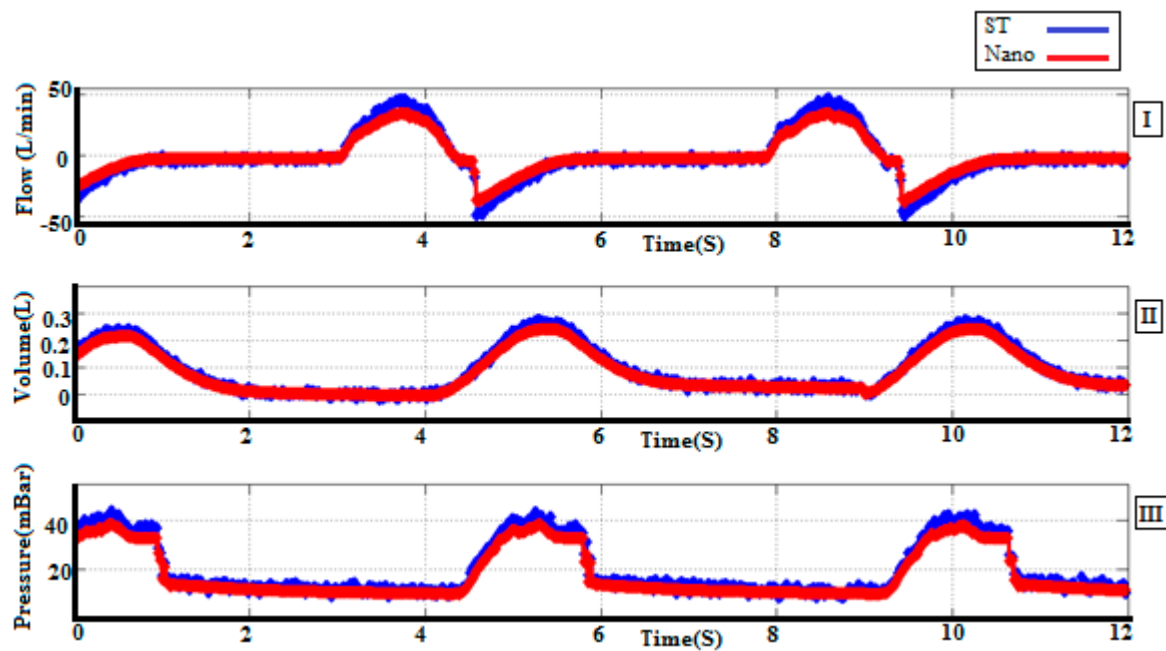


Figure 39. Control of respiratory variables made in Huancayo, Peru.

In Figure 39II the curves of the controlled volume (implicit) and measured by the designed ST (blue colour curve) as well as the volume measured by the designed ST enhanced by nanostructures (red colour curve) are presented, with a steady state error of 1.5% of the ST and 0.7% of the ST enhanced by nanostructures.

Furthermore, in Figure 39III the curves of the controlled pressure (implicit) and measured by the designed ST (blue colour curve) as well as the pressure measured by the designed ST enhanced by nanostructures (red colour curve) are shown, with a steady state error of 1.8% for the ST and 0.8% for the ST enhanced by nanostructures.

Therefore, the designed ST of nanostructures (TiO_2 nanotubes) based on Anodic Aluminium Oxide (AAO) provided better results in robustness, response time and resolution, which supported measurements from the approximated range of operation between 0.985 atm (Lima) and 1 atm (Huancayo).

6. Conclusions

A sensor/transducer (ST) was designed to measure the pressure difference through an orifice plate and to obtain the airflow rate, volume and pressure over time to register the performance of mechanical ventilators. The geometrical characteristics of the proposed sensor based on an orifice plate were researched in order to identify the appropriate parameters to measure the physical variables. The diameter has an important influence on the performance of the sensor; in this sense, a diameter of 8 mm provides the optimal response, in terms of magnitudes and tracking, for the mechanical ventilator curves without significantly increasing the pressure inlet for the breathing circuit which is provided by the mechanical ventilator. A diameter in the range of 4 mm to 6 mm can achieve the pressure difference of airflow, but with a nonlinear response and for the range between 10 mm and 12 mm, the ST can measure the physical variables in linear responses for breathing values (it can be used to measure airflow shared by several patients connected to one mechanical ventilator as a future application). Therefore, it was suggested to use the ST with a diameter of 8 mm due to its linear response and robustness under disturbances.

The mathematical model of the system was designed and evaluated. Consequently, an algorithm was also designed to obtain the airflow, volume and pressure from the pressure

difference, which were obtained by the transduction process of the transducer joined to the designed sensor. Moreover, the ST system was analyzed in dynamical and transient behavior for ranges of work that depended on geometrical parameters and physical values of airflow, pressure, and volume of mechanical ventilators for artificial human breathing. This is a novel proposed sensor design such as other new proposals [22–24] because of the multiple variable correlation also variables considered like disturbances (temperature and vibration) and considering the effect of nanostructures in this objective.

For a given orifice diameter, a correlation was observed between the pressure difference and the airflow. This correlation was not linear, but instead showed a parabolic tendency. Secondly, similar results and tendencies were observed between the steady-state and transient-state simulations. Therefore, it can be concluded that a steady-state approach (and its corresponding assumptions) can be considered to validly describe the transient behavior of this orifice plate sensor.

For a given flow, the smaller the orifice diameter, the larger the pressure difference induced in the orifice plate. This could happen because, for a given flow, a smaller orifice diameter requires the flow to pass through the opening. This increases the flow velocity, but at the cost of reducing the flow pressure at the outlet, resulting in greater pressure differences in the orifice plate. Therefore, a bigger inlet pressure would be necessary to help the flow overcome the pressure loss in the pipes. It can also be concluded that a plate with a smaller orifice diameter would be the best for this sensor. Taking this into account, lower pressure drops would occur in the plate, which would not considerably affect the flow, while at the same time being large enough to be detected by the ST and still being in the measuring range.

The designed ST enhanced by nanostructures of anodic aluminium oxide can provide a faster and robust response for geographic conditions where the atmospheric pressure level is different, as was the case in this research (tests in Lima and Huancayo). The nanostructure samples used for the designed sensors have the potential to fix adaptive coefficients to improve the operating work and enhance the response system (breathing variables) in case of disturbances.

Author Contributions: Conceptualization, J.A.C.C., C.G.R.R. and J.J.J.d.C.y.F.; methodology, J.A.C.C. and C.G.R.R.; software, J.A.C.C., J.H.L.J., C.G.R.R., B.J.M.A.C., S.C.A. and J.J.J.d.C.y.F.; validation, J.A.C.C. and A.T.H.; formal analysis, J.A.C.C., C.G.R.R. and S.C.A.; investigation, J.A.C.C., C.G.R.R. and A.M.G.A.; resources, J.A.C.C., C.G.R.R. and S.C.A.; data curation, J.A.C.C. and J.H.L.J.; writing—original draft preparation, J.A.C.C. and C.G.R.R.; writing—review and editing, J.A.C.C., C.G.R.R., A.M.G.A. and J.J.J.d.C.y.F.; visualization, J.A.C.C. and C.G.R.R.; Transduction mathematical and algorithm design and nanostructure design J.A.C.C. Supervision, J.A.C.C., J.H.L.J., C.G.R.R. and J.J.J.d.C.y.F.; project administration, J.J.J.d.C.y.F. and A.M.G.A.; funding acquisition, J.J.J.d.C.y.F. All authors have read and agreed to the published version of the manuscript.

Funding: This work was supported by CONCYTEC-FONDECYT based on the contest “PROYECTOS ESPECIALES: Modalidad-Escalamiento de proyectos COVID-19” [74169], to Pontificia Universidad Católica del Perú, to Prototy and MODASA.

Institutional Review Board Statement: Not applicable.

Informed Consent Statement: Not applicable.

Data Availability Statement: Not applicable.

Acknowledgments: The authors would like to express their special gratitude to the Prototy team, who shared their knowledge and experience of the OxyGEN project development. Furthermore, the authors would like to acknowledge the OxygenIPPE team, including Andrea Portal, Juan José Leyton and Romel Rosales who devised and assisted in the design of the components inside the mechanical ventilator, Broni Huamaní and Giovani Berrospi who assisted in the transduction stage, experimental tests and sensors assembly, Joaquin Gonzales who developed the electronic display for displaying the ventilation parameters for medical staff and Cristian Rimac who assisted in the schematic representations. Furthermore, we express our gratitude to the Alexandr Hinostraza, because of his medical analysis suggestions during the design and analysis of the experimental data.

Gratitude is also expressed to the researchers of the Metrology Laboratory PUCP, due to their support in the experimental analysis, as well as acknowledgement to the Mechanical Department of PUCP due to the support given to use measurement equipment for the experiments.

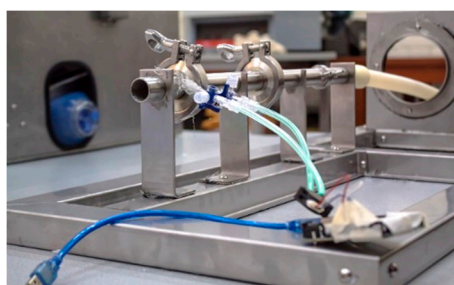
Conflicts of Interest: The authors declare no conflict of interest. The funders had no role in the design of the study; in the collection, analyses, or interpretation of data; in the writing of the manuscript, or in the decision to publish the results.

Appendix A

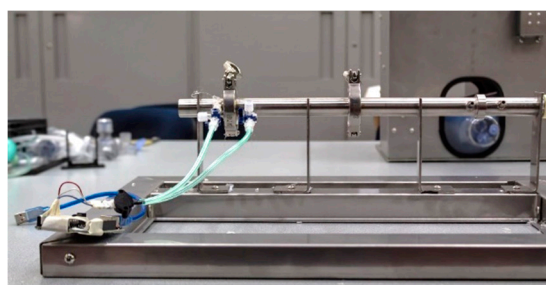
This appendix describes the special equipment designed for the validation and mathematical characterization of the air flow sensor in different working conditions of air flow and the low-cost mechanical ventilator based on cams where the air flow sensor was installed.

Appendix A.1. Steady State Air Flow Test Bench

In order to determine the optimal orifice diameter for the medical flow sensor in stationary conditions, a test bench was specially designed for this experiment (Figure A1). The holders of the sensor can be seen in the diagonal view (Figure A1a) and the side view (Figure A1b) of the test bench, which are quite important due to keep the correct position of the sensor during the experiments. It consists of a pipe where an air flow is induced by an air compressor, a fixed orifice plate to the pipe for flow measurement and a variable orifice-plate flow sensor. The fixed orifice plate was calibrated with a medical gas flow meter Fluke VT650 in a validation laboratory implemented in the COVID19-pandemic context at the Pontificia Universidad Católica del Perú. This fixed orifice-plate can help to determine the real flow through the variable orifice-plate flow sensor. In this sense, the orifice diameter can be changed and the relation between real flow and pressure difference can be obtained.



(a)



(b)

Figure A1. Air flow test bench designed for model validation.

Appendix A.2. Mechanical Ventilation System Oxygen IP.PE

OxygenIP.PE is a low-cost functional mechanical ventilation prototype based on cams [1] OxyGEN-IP, which was developed by Protofy [6]. A redesign was carried out according to the special requirements and available technology in Peru; however, the working concept (compression mechanism) established by Protofy was maintained due to the satisfactory results [25]. Figure A2 shows the OxygenIP.PE mechanical ventilator. Its working concept consists of an air bag compression mechanism based on cams to produce a pressure increment inside the cam and then air flow to the patient through a breathing circuit. Moreover, it can work with five different cams depending on the air volume requirement for a particular patient.



Figure A2. Mechanical ventilation system OxygenIP.PE, where the novel air low sensor/transducer is implemented.

Appendix B

In this research, it was necessary to work with strategies of Model Predictive Control (MPC) to join both subsystems (mechanical and electrical) for the main algorithm, for which an internal identification system was used, while adaptive control coefficients/weights searched for the right control. Therefore, the nonlinear function “*g*” and internal variables “*z(t)*” due to excitation “*v(t)*” as a function of time “*t*” were important.

$$\frac{dx(t)}{dt} = g(z(t)v(t), \theta) \tag{A1}$$

On the other hand, “*m(t)*” correlated with “*z(t)*” and “*v(t)*” through a nonlinear function “*n*”.

$$m(t) = n(z(t), v(t), \theta) \tag{A2}$$

Additionally, “*A_s*” represents trajectory and the input excitation “*O*” is included depending of the sample time *k_i*.

$$A_s^T = (111 \dots 11111)O(k_i) \tag{A3}$$

So, the costing function “*J*” was analyzed to achieve the optimal desired response [21].

$$J = (A_s - Y)^T (A_s - Y) + \Delta S^T A \Delta S \tag{A4}$$

In which the expected response is

$$Y = LX(k_i) + \phi \Delta S \tag{A5}$$

Otherwise,

$$J = (A_s - LX(k_i))^T (A_s - LX(k_i)) - 2\Delta S^T \phi^T (A_s - LX(k_i)) + \Delta U^T (\phi^T \phi + A) \Delta S \tag{A6}$$

where “*L*” and “*φ*” are matrices that contain all the physical parameters of the system (as joining matrices above for the identified result) [21].

$$\frac{\partial J}{\partial \Delta S} = -2\phi^T (A_s - LX(k_i)) + 2(\phi^T \phi + R) \Delta S \tag{A7}$$

So

$$\frac{\partial J}{\partial \Delta S} = 0 \tag{A8}$$

From which the optimal excitation signal in order to find the optimal response is given by [1,21]

$$\Delta S = (\phi^T \phi + A)^{-1} \phi^T (A_S - LX(k_i)) \quad (\text{A9})$$

References

1. Calderón Ch, J.A.; Rincón, C.; Agreda, M.; Jiménez de Cisneros, J.J. Design and Analysis of a Mechanical Ventilation System Based on Cams. *Heliyon* **2021**, *7*, e08195. [CrossRef] [PubMed]
2. Freescale Semiconductor Literature Distribution Center, Inc. *Ventilator/Respirator Hardware and Software Design Specification*; Freescale Semiconductor Literature Distribution Center, Inc.: Denver, CO, USA, 2011; pp. 11–20.
3. Brzeski, P.; Lazarek, M.; Perlikowski, P. Experimental study of the novel tuned mass damper with inerter which enables changes of inertance. *J. Sound Vib.* **2017**, *404*, 47–57. [CrossRef]
4. Fowles, G.; Boyes, W. *Measurement of Flow*, 4th ed.; Elsevier: Amsterdam, The Netherlands, 2010; ISBN 978075068308.
5. Biselli, P.J.C.; Nóbrega, R.S.; Soriano, F.G. Nonlinear flow sensor calibration with an accurate syringe. *Sensors* **2018**, *18*, 2163. [CrossRef] [PubMed]
6. OxyGEN Project. Available online: <https://www.oxygen.protofy.xyz/download> (accessed on 23 November 2020).
7. Chang, J.; Acosta, A.; Aspiazú, J.B.; Reategui, J.; Rojas, C.; Cook, J.; Nole, R.; Giampietri, L.; Pérez-Buitrago, S.; Casado, F.L.; et al. Masi: A mechanical ventilator based on a manual resuscitator with telemedicine capabilities for patients with ARDS during the COVID-19 crisis. *HardwareX* **2021**, *9*, e00187. [CrossRef] [PubMed]
8. Jamróz, P. Interaction between the Standard and the Measurement Instrument during the Flow Velocity Sensor Calibration Process. *Processes* **2021**, *9*, 1792. [CrossRef]
9. Włodarczak, S.; Ochowiak, M.; Doligalski, M.; Kwapisz, B.; Krupińska, A.; Mrugalski, M.; Matuszak, M. Flow Rate Control by Means of Flow Meter and PLC Controller. *Sensors* **2021**, *21*, 6153. [CrossRef] [PubMed]
10. Koirala, N.; McLennan, G. Mathematical Models for Blood Flow Quantification in Dialysis Access Using Angiography: A Comparative Study. *Diagnostics* **2021**, *11*, 1771. [CrossRef] [PubMed]
11. Bisgaard, J.; Tajsoliman, T.; Muldbak, M.; Rydal, T.; Rasmussen, T.; Huusom, J.K.; Gernaey, K.V. Automated Compartment Model Development Based on Data from Flow-Following Sensor Devices. *Processes* **2021**, *9*, 1651. [CrossRef]
12. Hammer, A.; Roland, W.; Zacher, M.; Praher, B.; Hanneschläger, G.; Löw-Baselli, B.; Steinbichler, G. In Situ Detection of Interfacial Flow Instabilities in Polymer Co-Extrusion Using Optical Coherence Tomography and Ultrasonic Techniques. *Polymers* **2021**, *13*, 2880. [CrossRef] [PubMed]
13. Landau, L.D.; Lifshitz, E.M. *Fluid Mechanics, Institute of Physical Problems*; U.S.S.R. Academy of Sciences: Moscow, Russia, 1987.
14. Aldoghaither, A.; Liu, D.-Y.; Laleg-Kirati, T.M. *Modulating Functions Based Algorithm for the Estimation of the Coefficients and Differentiation Order for a Space-Fractional Advection-Dispersion Equation*; Society for Industrial and Applied Mathematics: Philadelphia, PA, USA, 2015.
15. Bridgeman, D.; Tsow, F.; Xian, X.; Forzani, E. A new differential pressure flow meter for measurement of human breath flow: Simulation and experimental investigation. *AIChE J.* **2016**, *62*, 956–964. [CrossRef] [PubMed]
16. Launder, B.E. MAN—ANSYS Fluent User’s Guide Release 15.0. *Knowl. Creat. Diffus. Util.* **2013**, *15317*, 724–746.
17. Paz, C.; Suárez, E.; Concheiro, M.; Porteiro, J. CFD transient simulation of a breathing cycle in an oral-nasal extrathoracic model. *J. Appl. Fluid Mech.* **2017**, *10*, 777–784. [CrossRef]
18. CLÍNICA BARCELONA. Available online: <https://www.clinicbarcelona.org/noticias/el-dispositivo-de-ventilacion-de-emergencia-desarrollado-por-clinic-germans-trias-i-pujol-y-ub-con-protofy-xyz-recibe-la-aprobacion-de-la-aemps-para-hacer-un-estudio-clinico> (accessed on 15 May 2020).
19. Karthik, G.S.Y.; Kumar, K.J.; Seshadri, V. Prediction of Performance Characteristics of Orifice Plate Assembly for Non-Standard Conditions Using CFD. *Int. J. Eng. Tech. Res.* **2015**, *3*, 2321–2869.
20. Funk, J.E.; Wood, D.J.; Chao, S.P. The transient response of orifices and very short lines. *J. Fluids Eng. Trans. ASME* **1972**, *94*, 483–489. [CrossRef]
21. Calderón, J.A.; Barriga, E.B.; Mas, R.; Chirinos, L.; Barrantes, E.; Alencastre, J.; Tafur, J.C.; Melgarejo, O.; Lozano, J.H.; Heinrich, B.; et al. Magnetic Bearing Proposal Design for a General Unbalanced Rotor System enhanced because of using sensors/actuators based in nanostructures. *E3S Web Conf.* **2019**, *95*, 01002. [CrossRef]
22. Халилов, И.А.; Керимов, С.Х.; Багирова, С.А.; Гаджиева, Ф., III. Синтез кулачкового механизма с учетом условий передачи сил и контактной прочности. (Khalilov, I.A.; Kerimov, S.K.; Bagirova, S.A.; Gadzhieva, F.S. Synthesis of a Cam Mechanism Taking into Account the Conditions for the Transfer of Forces and Contact Strength). 2017. Available online: <http://web.iyte.edu.tr/~{gokhankiper/ISMMS/Khalilov.pdf> (accessed on 6 April 2022).
23. Liang, L.; Qin, K.; El-Baz, A.S.; Roussel, T.J.; Sethu, P.; Giridharan, G.A.; Wang, Y. A Flow Sensor-Based Suction-Index Control Strategy for Rotary Left Ventricular Assist Devices. *Sensors* **2021**, *21*, 6890. [CrossRef] [PubMed]
24. Algarni, M. Optimization of Nano-Additive Characteristics to Improve the Efficiency of a Shell and Tube Thermal Energy Storage System Using a Hybrid Procedure: DOE, ANN, MCDM, MOO, and CFD Modeling. *Mathematics* **2021**, *9*, 3235. [CrossRef]
25. Melaibari, A. Free Vibration of FG-CNTRCs Nano-Plates/Shells with Temperature-Dependent Properties. *Mathematics* **2022**, *10*, 583. [CrossRef]